NASA
Technical
Paper
3331

October 1993

Effects of Window Size and Shape on Accuracy of Subpixel Centroid Estimation of Target Images

Sharon S. Welch

NASA

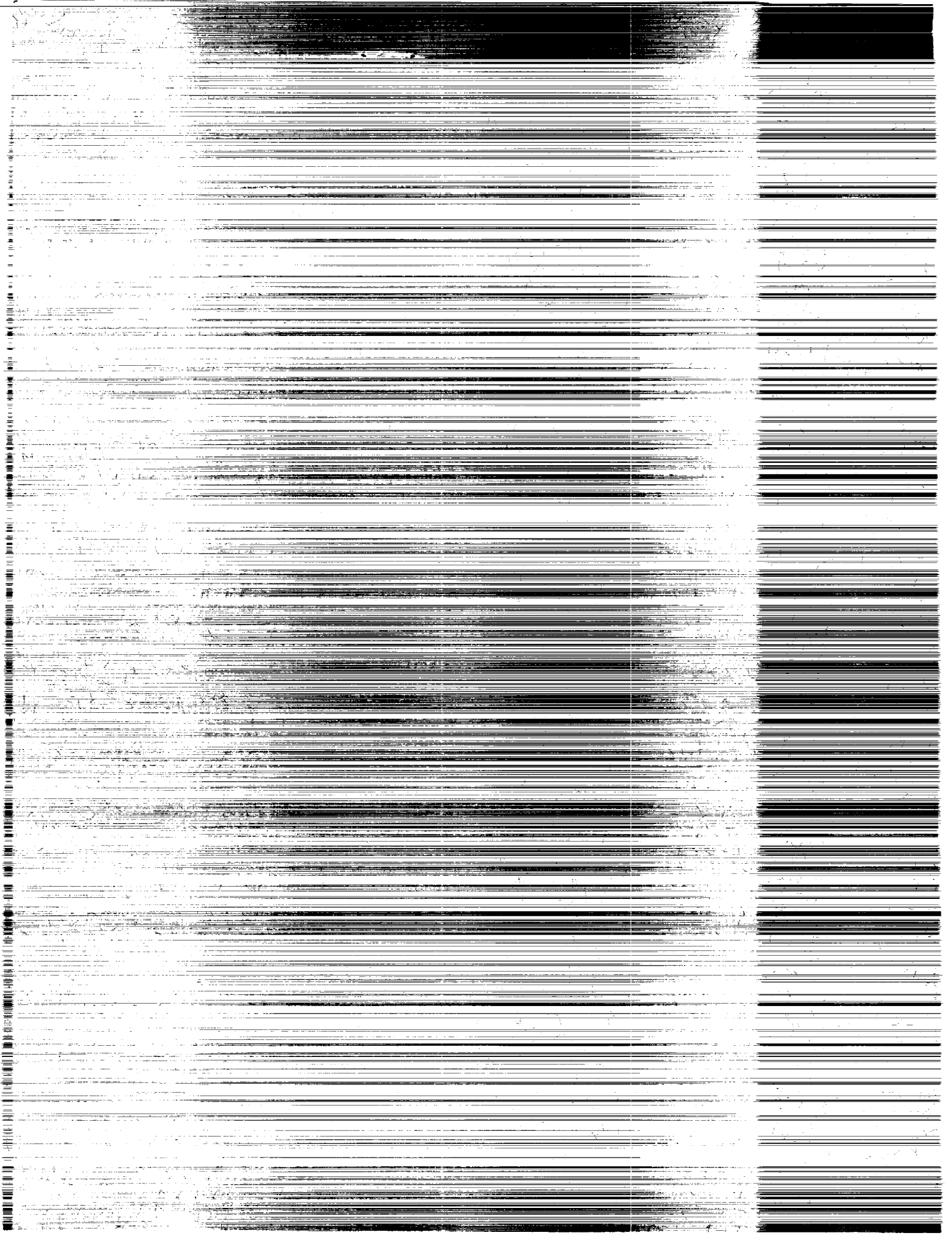

NASA Technical Paper 3331

1993

Effects of Window Size and Shape on Accuracy of Subpixel Centroid Estimation of Target Images

Sharon S. Welch
Langley Research Center
Hampton, Virginia

National Aeronautics and Space Administration
Office of Management
Scientific and Technical Information Program

Abstract

A new algorithm is presented for increasing the accuracy of subpixel centroid estimation of (nearly) point target images in cases where the signal-to-noise ratio is low and the signal amplitude and shape vary from frame to frame. In the algorithm, the centroid is calculated over a data window that is matched in width to the image distribution. Fourier analysis is used to explain the dependency of the centroid estimate on the size of the data window, and simulation and experimental results are presented which demonstrate the effects of window size for two different noise models. The effects of window shape have also been investigated for uniform and Gaussian-shaped windows. The new algorithm has been developed to improve the dynamic range of a close-range photogrammetric tracking system that provides feedback for control of a large gap magnetic suspension system (LGMSS).

Introduction

Centroid-estimation algorithms have long been used in digital imaging to locate target images to subpixel accuracies. Applications of centroid estimation include star tracking (ref. 1), point and edge detection for machine vision (ref. 2), close-range photogrammetry (ref. 3), and motion analysis. The effects of sampling and noise on the accuracy of the centroid estimate for point source images, images of extended sources, and edge detection have been analyzed previously and documented by several authors (refs. 4 to 8). The systematic errors due to undersampling that have been described for centroid estimation are common to all interpolation algorithms and have been analyzed from the point of view of performing image reconstruction (refs. 9 and 10). In these previous analyses, experimental approaches as well as analytical approaches based on Fourier techniques have been used to quantify the errors due to noise, quantization, and sample spacing. To date, the effect of window size on the accuracy of subpixel centroid estimation has been limited to a qualitative analysis derived from experiments that measured the error in centroid estimation as a function of different N-point algorithms (ref. 4).

In this paper, Fourier techniques are used to analyze the dependency of the systematic error on window size. In addition, the effects of window size and shape on subpixel centroid-estimation accuracy in the presence of noise are studied. It is shown that there can be an advantage to using a shaped window for centroid estimation of point target images for signals that vary in amplitude and width, provided the pixel-to-pixel noise is independent of signal amplitude. A brief review of the effects of the optical point spread function (PSF), target size, and sample spacing on systematic error is provided in order to compare and contrast these effects with those attributable to the data window. Quantization effects, however, are not addressed in this paper.

In many applications involving centroid estimation, the signal shape and amplitude are either controllable or fixed. In these cases, the optimum sample spacing and window size relative to the target image distribution are known a priori, and a correction can be applied for systematic errors (ref. 7). In other applications where the noise is small or the image is averaged over several frames, a larger window (relative to the distribution) can be used in the centroid calculation. This eliminates systematic errors arising because of truncation of the signal. In the application discussed in this paper, centroid estimation is used to locate images of point targets along a linear charge-coupled device (CCD) detector, where the signal-to-noise ratio is small and, because the targets are moving, the (one-dimensional) images vary in size and amplitude. For these reasons, it is not possible to apply a correction for the systematic errors or to calculate the centroid using a large fixed data window.

The application discussed herein is the optical measurement system (OMS) for the large gap magnetic suspension system (LGMSS) (fig. 1). In the OMS, small infrared light-emitting diode (LED) targets have been embedded in the top surface of a rigid cylindrically shaped element that contains a permanent magnet core. The element is magnetically levitated above a planar array of electromagnets. Sixteen linear CCD cameras arranged in pairs are located symmetrically about and above the levitated cylinder. A total of eight targets are located along the top surface of the cylinder (fig. 2), and the targets are multiplexed in time for target identification. Triangulation techniques are used to determine the

position and attitude of the levitated cylinder from the locations of the projected target images in the 16 cameras. The position and attitude information is supplied to the electromagnet controller to stabilize levitation of the cylinder and to control motion in six degrees of freedom.

The position and attitude of the cylinder are determined using weighted least squares. An estimate of the error in each computed centroid value is passed along with the centroid value and is used to establish a weighting factor for the particular camera measurement. In order to achieve the required accuracy in the estimate of position and attitude, it is necessary to locate the centroids of at least 6 of the target images to 1/15 of a pixel in a minimum of 12 of the 16 cameras. As the cylinder, and hence each target, moves over the field of view, both the amplitude and the width of the target images vary (fig. 3). If the centroid location of a target image is determined with a fixed window size (which is the same for all 16 cameras), and the window size is optimum for those image distributions falling in the midrange of possible values, then as the target images vary in amplitude and width, the error in the centroid estimate grows for those images for which the distribution falls outside the midrange. Thus, with a fixed window size, the accuracy of the centroid estimate falls off because of noise or systematic error, and the accuracy of the position and attitude estimate correspondingly decreases.

In order to increase the dynamic range of the system, an algorithm has been developed to adjust the width of the centroid window as the light intensity distribution of the image varies. This algorithm provides the minimum error in centroid estimation over the maximum range of signal amplitude and shape. This paper analyzes the dependency of systematic and noise-induced errors on the size and shape of the data window. Experimental results are presented and compared with the results of numerical simulations.

The following analysis is limited to one spatial dimension. It is assumed that the PSF of the imaging optics can be approximated by a Gaussian function. Because a two-dimensional Gaussian function is separable in x and y, the results of the one-dimensional analysis can readily be extended to two dimensions.

Symbols and Abbreviations

b	half-width of Gaussian distribution used to simulate the optical point spread of the imaging optics
$\mathrm{comb}(x/x_s)$	sampling function
$f(x)$	light intensity distribution of one-dimensional target image
$F(\xi)$	Fourier transform of $f(x)$
$\widetilde{F}(\xi)$	$= F(\xi)R(\xi)$
F_{RW}	$= FR * W$
$F_{SW}(\xi)$	Fourier transform of $f_{SW}(x)$
$F'_{SW}(\xi)$	first derivative of $F_{SW}(\xi)$ with respect to ξ
$f_{SW}(x)$	sampled and windowed version of $f(x)$
$g(x - x_o)$	one-dimensional light intensity distribution of target located at x_o
$H(\xi)$	general function of ξ
N	number of pixels corresponding to half the window width
$\mathrm{PSF}(x)$	point spread function of imaging optics
$R(\xi)$	Fourier transform of $r(x)$
$r(x)$	pixel response function
$T(\xi)$	general function of ξ
$W(\xi)$	Fourier transform of $w(x)$
$w(x)$	window function
x	spatial variable
$\bar{x}$	centroid of continuous one-dimensional light intensity distribution
x_c	amount by which $f(x)$ is shifted with respect to the sampling grid
x_p	pixel location of the peak signal
x_s	sample spacing
$\bar{x}_{SW}$	centroid of $f_{SW}(x)$
ϵ_c	systematic error, $\bar{x} - \bar{x}_{SW}$
ξ, η, μ	variables of integration
Abbreviations:	
CCD	charge-coupled device
LED	light-emitting diode
rms	root-mean-square
SNR	$= \frac{\text{Peak signal}}{\text{Standard deviation of background signal}}$

A prime on a symbol denotes the first derivative. An asterisk used as an operational sign denotes convolution of the quantities.

Effect of Window Size on Systematic Error

The objective is to produce a minimum error estimate of the centroid of a one-dimensional light intensity distribution corresponding to a (nearly) point target image. The target image will have been sampled and only a portion of the sampled distribution (those points lying within the window) will have been used in the calculation. By definition, the centroid of the continuous one-dimensional light intensity distribution is given by

$$\bar{x} = \frac{\int_{-\infty}^{\infty} x f(x)\, dx}{\int_{-\infty}^{\infty} f(x)\, dx} \tag{1}$$

where $\bar{x}$ is the centroid, $f(x)$ is the light intensity distribution of the image, and x is the position. This equation may be expressed in terms of $F(\xi)$, the Fourier transform of $f(x)$, as

$$\bar{x} = \left[\frac{dF(\xi)/d\xi}{-2\pi i F(\xi)}\right]_{\xi=0} \tag{2}$$

where

$$F(\xi) = \int_{-\infty}^{\infty} f(x) \exp(-2\pi i \xi x)\, dx \tag{3}$$

The effect of using only a portion of the image distribution, that is, of placing a window about the distribution, is to spread the energy in the spectrum of $F(\xi)$ into higher frequencies. This effect is shown in figure 4. When the image distribution is both windowed and sampled, as it is in practice, the width of the window relative to the width of $f(x)$ and the sample spacing is important.

In a CCD array, an image is sampled at discrete intervals with an array of detectors or pixels. Each pixel has a response that is spatially distributed over the width of the pixel. If $f(x)$ is the function that represents the continuous light intensity distribution of the image, then sampling with a CCD array can be modelled mathematically as a convolution of $f(x)$ with a function $r(x)$, which represents the spatial response of each pixel, followed by a multiplication of the resulting product with the sampling function $\mathrm{comb}(x/x_s)$, where

$$\frac{1}{x_s}\mathrm{comb}(x/x_s) = \sum_{n=-\infty}^{\infty} \delta(x - n x_s)$$

and x_s is the sample spacing of the pixels. This convolution and multiplication results in a sampled data set that is of infinite extent. In order to reproduce the real data set, which is of limited extent, the sampled function is multiplied by a window function $w(x)$ of finite width. If the sampled and windowed function is defined as $f_{SW}(x)$, then

$$f_{SW} = (f * r)\left(\frac{1}{x_s}\mathrm{comb}\right) w \tag{4}$$

where the asterisk denotes the convolution (pp. 284 and 285 of ref. 11). From equations (3) and (4) it follows that the Fourier transform of $f_{SW}(x)$ is

$$\begin{aligned} F_{SW} &= \widetilde{F} * \mathrm{comb} * W \\ &= (\widetilde{F} * W) * \mathrm{comb} \end{aligned}$$

where

$$\mathrm{comb} = \sum_{n=-\infty}^{\infty} \delta\left(\xi - \frac{n}{x_s}\right)$$

and

$$\widetilde{F} = FR$$

Thus,

$$F_{SW}(\xi) = \sum_{n=-\infty}^{\infty} F_{RW}\left(\xi - \frac{n}{x_s}\right) \tag{5}$$

where

$$F_{RW} = \widetilde{F} * W \tag{6}$$

Equation (5) shows that the spectrum of the sampled and windowed function is the sum of the individual spectra F_{RW} repeated at intervals of $1/x_s$. Figure 5 shows a representative sampled and windowed function $f_{SW}(x)$ and the corresponding Fourier transform $F_{SW}(\xi)$. As for the continuous distribution case, placing a window about the image distribution can broaden F_{RW}. When the image is both windowed and sampled this spread can result in energy spillover from neighboring transforms. If the window width is too small relative to the width of the signal and the sample spacing, then systematic error is introduced into the centroid estimate as energy from higher orders spills into $F_{RW}(0)$.

Before the specific form of the error introduced by the data window is discussed, the effects of the optical PSF, pixel response function, and target size are briefly reviewed in order to distinguish between those errors that are due to undersampling and those errors that are due to the finite extent of the data.

A Review of Effects of Optical PSF, Pixel Response Function, and Target Size

As has been shown previously (refs. 4, 7, 9, and 10), the form of the subpixel error in centroid

estimation and image reconstruction due to undersampling is a sinusoidal function of the position of the "true" centroid or image location with respect to the sample grid (fig. 6). The magnitude of this error is a function of the widths of the optical PSF, pixel response function, and target.

In a digital imaging system, the optical PSF describes the degree to which the target image is blurred because of the limits of diffraction in the imaging optics. Provided the imaging optics are shift invariant, then the light intensity distribution of the image $f(x - x_o)$ is the convolution of $g(x - x_o)$ with the PSF of the imaging optics, where $g(x - x_o)$ is the light intensity distribution of the true target and x_o is the location of the centroid of the distribution. (See pp. 335 and 336 of ref. 11.)

Because the optics tend to blur, or smear out the image of the target, the PSF has an inverse effect on the Fourier transform of the image. That is, the Fourier transform of the blurred image is narrower than the Fourier transform of the true image of the target. For this reason, as shown in references 4 and 6 to 8, the systematic error in centroid estimation, or image reconstruction, due to undersampling decreases as the width of the PSF of the imaging system increases.

Similarly, the pixel response function $r(x)$ spreads the sampled image distribution. This spreading is shown in equation (4), where $r(x)$ is convolved with $f(x)$, or equivalently in equation (6), where $F(\xi)$ is multiplied by $R(\xi)$. For the linear CCD array detector that was used to generate the experimental results discussed in this paper, the width of the pixel response function is approximately equal to $0.8x_s$.

The size of the target also affects the amplitude of the undersampling error. Typically, the larger the target relative to the sample spacing, the smaller the systematic error. However, the amplitude of the undersampling error does not decrease monotonically with increasing target width. Rather, for a fixed pixel response function, if the amplitude of the error is plotted as a function of target size, then the resulting graph shows this amplitude to be modulated periodically with target size (refs. 5 and 8). This periodicity can be understood by looking at the graphs of figure 7, wherein simulated functions $f(x)$ and $F(\xi)$ are plotted for two different target widths, x_s and $4x_s$ (uniform amplitude). The PSF (fig. 7 (a)) is assumed to be of the form

$$\mathrm{PSF}(x) = \exp\left[-\pi\left(\frac{x}{bx_s}\right)^2\right] \tag{7}$$

As is evident in the graphs of figures 7(b) to 7(d), if the target is uniform in intensity and has sharp discontinuities at the edges, then the Fourier transform of the true target image looks like a sinc function (fig. 7(d)). As the width of the target changes for a fixed PSF and pixel response function, the side lobes move relative to zero frequency. For some target sizes and PSF's, $F(\xi)$ and $F'(\xi)$ are zero; for others, $F'(\xi)$ is between zero and a peak of the side lobes. The result of this is that the amplitude of the sinusoidal error as a function of target size is modulated in a periodic fashion that is determined by the ratio of the width of the target to the sample spacing.

Centroid-Estimation Error for Sampled and Windowed Function

From equation (2), the estimate of the centroid of the sampled and windowed function $f_{SW}(x)$ is

$$\bar{x}_{SW} = \frac{F'_{SW}(0)}{-2\pi i F_{SW}(0)} \tag{8}$$

With the systematic error ϵ_c defined as the difference between $\bar{x}$ and $\bar{x}_{SW}$, then from equations (2) and (8)

$$\epsilon_c = \bar{x} - \bar{x}_{SW} = -\frac{1}{2\pi i}\left[\frac{F'(0)}{F(0)} - \frac{F'_{SW}(0)}{F_{SW}(0)}\right] \tag{9}$$

Substituting equation (5) for $F_{SW}(\xi)$ yields

$$\epsilon_c = -\frac{1}{2\pi i}\left[\frac{F'(\xi)}{F(\xi)} - \frac{(d/d\xi)\sum_{n=-\infty}^{\infty} F_{RW}\left(\xi - (n/x_s)\right)}{\sum_{n=-\infty}^{\infty} F_{RW}\left(\xi - (n/x_s)\right)}\right]_{\xi=0} \tag{10}$$

Using the approach introduced in reference 7, and assuming that the distribution of the target image is an even function about a point that is shifted an amount x_c with respect to the sampling grid, results in

$$f(x) = f_e(x - x_c)$$

and

$$F(\xi) = \exp(-2\pi i x_c \xi) F_e(\xi)$$

Carrying this analysis further, the effect of the window on the Fourier transform $F(\xi)$ is, as shown by equation (6), a convolution of the Fourier transform of the window function $W(\xi)$ with $\widetilde{F}(\xi)$, or

$$F_{RW} = \widetilde{F} * W = \left[\exp(-2\pi i x_c \xi)\widetilde{F}_e\right] * W = \int_{-\infty}^{\infty} \exp(-2\pi i x_c \eta)\widetilde{F}_e(\eta) W(\xi - \eta)\, d\eta \tag{11}$$

To see the effect of the window on the error ϵ_c, we return now to equation (10) and solve for $F'_{RW}(\xi)$ using equation (11) and the following relationship:

$$\int_{-\infty}^{\infty} T(\eta) H(\xi - \eta)\, d\eta = \int_{-\infty}^{\infty} T(\xi - \eta) H(\eta)\, d\eta$$

This yields

$$F_{RW}(\xi) = \int_{-\infty}^{\infty} \exp\left[-2\pi i x_c(\xi - \eta)\right] \widetilde{F}_e(\xi - \eta) W(\eta)\, d\eta$$

and

$$\begin{aligned} F'_{RW}(\xi) &= \frac{d}{d\xi}\int_{-\infty}^{\infty} \exp\left[-2\pi i x_c(\xi - \eta)\right] \widetilde{F}_e(\xi - \eta) W(\eta)\, d\eta \\ &= -2\pi i x_c \int_{-\infty}^{\infty} \exp\left[-2\pi i x_c(\xi - \eta)\right] \widetilde{F}_e(\xi - \eta) W(\eta)\, d\eta \\ &\quad + \int_{-\infty}^{\infty} \exp[-2\pi i x_c(\xi - \eta)] \widetilde{F}'_e(\xi - \eta) W(\eta)\, d\eta \end{aligned}$$

Plugging these values for $F_{RW}(\xi)$ and $F'_{RW}(\xi)$ into equation (10), setting $\xi = 0$, and cancelling like terms in the numerator and denominator leaves

$$\epsilon_c = \frac{1}{2\pi i} \frac{\sum_{n=-\infty}^{\infty} \left(\int_{-\infty}^{\infty} \exp\left\{-2\pi i x_c[-\eta - (n/x_s)]\right\} \widetilde{F}'_e[-\eta - (n/x_s)] W(\eta)\, d\eta\right)}{\sum_{n=-\infty}^{\infty} \left(\int_{-\infty}^{\infty} \exp\left\{-2\pi i x_c[-\eta - (n/x_s)]\right\} \widetilde{F}_e[-\eta - (n/x_s)] W(\eta)\, d\eta\right)} \tag{12}$$

If we assume that the window is an odd number of pixels, then $W(\xi)$ is an even function. Furthermore, if one makes the assumption that the pixel response function is symmetric about the center of the pixel, then

$R(\xi)$ is also an even function. Rearranging terms in the numerator and denominator of equation (12) and realizing that $\widetilde{F}_e'$ is an odd function yields

$$\epsilon_c = \frac{1}{2\pi}\left(\frac{-\int_{-\infty}^{\infty}\sin(2\pi x_c\eta)\widetilde{F}_e'(\eta)W_e(\eta)\,d\eta + 2\sum_{n=1}^{\infty}\left\{\int_{-\infty}^{\infty}\sin(2\pi x_c\mu)\widetilde{F}_e'(\mu)W_e[(n/x_s)-\mu]\,d\mu\right\}}{\int_{-\infty}^{\infty}\cos(2\pi x_c\eta)\widetilde{F}_e(\eta)W_e(\eta)\,d\eta + 2\sum_{n=1}^{\infty}\left\{\int_{-\infty}^{\infty}\cos(2\pi x_c\mu)\widetilde{F}_e(\mu)W_e[(n/x_s)-\mu]\,d\mu\right\}}\right) \tag{13}$$

where

$$\int_{-\infty}^{\infty}\cos(2\pi x_c\mu)\widetilde{F}_e'(\mu)W_e(\mu)\,d\mu = 0$$

and

$$\int_{-\infty}^{\infty}\sin(2\pi x_c\mu)\widetilde{F}_e(\mu)W_e(\mu)\,d\mu = 0$$

because the integral of an odd function times an even function evaluated over even limits is zero. The first integral in the denominator of equation (13) is generally much larger than the second integral, and therefore

$$\epsilon_c \approx \frac{1}{2\pi}\left(\frac{-\int_{-\infty}^{\infty}\sin(2\pi x_c\eta)\widetilde{F}_e'(\eta)W_e(\eta)\,d\eta + 2\sum_{n=1}^{\infty}\left\{\int_{-\infty}^{\infty}\sin(2\pi x_c\mu)\widetilde{F}_e'(\mu)W_e[(n/x_s)-\mu]\,d\mu\right\}}{\int_{-\infty}^{\infty}\cos(2\pi x_c\eta)\widetilde{F}_e(\eta)W_e(\eta)\,d\eta}\right) \tag{14}$$

When the window is large, $W_e(\xi) \to \delta(\xi)$ and equation (14) reduces to

$$\epsilon_c \approx \frac{1}{\pi}\frac{\sum_{n=1}^{\infty}\sin(2\pi x_c n/x_s)\widetilde{F}_e'(n/x_s)}{\widetilde{F}_e(0)}$$

Because of the frequency cutoff of the optics, the $n = 1$ term dominates. Thus, the form of the systematic error in this case is sinusoidal with an amplitude proportional to $\widetilde{F}_e'(1/x_s)$.

However, when the width of the window is approximately the same as the width of the image distribution, the convolution integrals of equation (14) spread each of the individual F_{RW} spectra and terms higher than the first become significant. As a result, the form of the subpixel error changes from a pure sinusoid to one period of a sawtooth plot (fig. 8). The sawtooth form corresponds to the systematic error that arises because of truncation of the signal. The amplitude of this error is now a function of the width of the window in addition to the widths of the pixel response function, the PSF, and the target.

A simulation was constructed to study the relationship between the shape and width of the window and the systematic error in centroid estimation. In all the simulations discussed herein, the target was assumed to be a point source, the PSF was assumed to be that given in equation (7), and the pixel response function was assumed to be uniform and of width x_s. Two different-shaped windows were simulated: (1) a uniform window, defined by

$$w(x) = \begin{cases} 1 & (x_p - Nx_s < x < x_p + Nx_s \text{ for } N = 1, 2, \ldots) \\ 0 & (\text{Otherwise}) \end{cases}$$

and (2) a Gaussian-shaped window defined by

$$w(x) = \begin{cases} \exp[-\pi(x - x_p^2)/(2Nx_s)^2] & (x_p - 2Nx_s < x < x_p + 2Nx_s \text{ for } N = 1, 2, \ldots) \\ 0 & (\text{Otherwise}) \end{cases}$$

where x_p is the pixel location of the peak signal. The functions $w(x)$ and corresponding Fourier transform $W(\xi)$ for the uniform and Gaussian-shaped windows are shown for comparison purposes in figure 9. Note that the Fourier transforms for both windows have a zero at approximately the same location. The width of the

Gaussian-shaped window has been chosen to provide a similar shape in frequency space to that of the uniform window. In addition, the error due to undersampling has been made negligibly small. Provided $b \geq 1.25x_s$, which was true for the cases that were simulated, the maximum error due to undersampling is less than 0.002 times the pixel spacing.

In figure 10, the simulation results show the predicted peak amplitude of the subpixel systematic error as a function of the ratio N/b for the two different-shaped windows. These results show that using a Gaussian-shaped window reduces the systematic error. The systematic error due to windowing goes to zero with the Gaussian-shaped window for values of N/b greater than approximately 1.0 and with the uniform window for values of N/b greater than approximately 2.5.

Effects of Window Size and Shape on Noise-Induced Error

In order to understand the effects of window size and shape on centroid-estimation error in the presence of noise, a simulation was constructed. Two different noise models were simulated. In one, the noise was modelled as a mean zero Gaussian random variable, independent of signal amplitude and independent for each pixel along the array. In the other, the noise was modelled as being proportional to the square root of the signal amplitude, where the proportionality factor was modelled as a mean zero Gaussian random variable. The reasons for selecting these two noise models are the following. Often in imaging applications the target signal is small relative to the background light, and the noise is considered to be background limited photon shot noise (BLIP). This case is simulated by the noise model in which the noise is independent of the signal and independent pixel to pixel. The other case closely approximates the characteristics of the sensor noise in the OMS.

Equation (7) was used to mathematically model the PSF of the optics. The source was modelled as a delta function with a peak signal of 1.0. A constant background signal was added to the target signal prior to addition of the noise. When the centroid was estimated, the values at the endpoints of the window were averaged, and this average value was subtracted from each signal value. This process simulated the threshold technique that is used on the OMS.

Simulations were run to determine the subpixel bias error and the standard deviation of the signal at any single subpixel position. To calculate the bias error, an average centroid estimate was calculated at each subpixel position and subtracted from the true centroid location. The average centroid estimate was taken to be the mean of 25 samples. The standard deviation of the centroid estimate at each subpixel location was also calculated.

The results of this simulation analysis are shown in figures 11 to 13. In figures 11(a) to 11(d), the average error over a single pixel is plotted as a function of x_c for representative samples of each combination of noise model and window shape. In figures 12(a) and 12(b), the rms value of the bias error over a single pixel is plotted as a function of the ratio N/b for the uniform window and the Gaussian-shaped window with the pixel-to-pixel noise independent. The rms error over the range $-0.5 < x_c < 0.5$ is defined as

$$\text{rms} = \sqrt{\frac{1}{P}\sum_{n=1}^{P}(\text{True centroid} - \text{Predicted centroid})^2}$$

where P is the total number of subpixel positions. In figures 12(c) and 12(d), similar plots are shown for the noise proportional to the square root of the signal amplitude. The different points correspond to different values of SNR in figures 12(a) and 12(b), where the SNR is defined as

$$\text{SNR} = \frac{\text{Peak signal}}{\text{Standard deviation of background signal}}$$

and to different standard deviations of the proportionality factor in figures 12(c) and 12(d). Figure 13(a) presents the standard deviations of the centroid estimates at single subpixel locations as a function of the SNR for the uniform and Gaussian-shaped windows and noise independent of signal amplitude. In figure 13(b), similar graphs are shown for the uniform and Gaussian-shaped windows and noise proportional to the square root of signal amplitude.

Four things become apparent from the simulation results, the first of which has been known for some time: (1) in the presence of noise, the standard deviation of the subpixel centroid estimate increases with increasing window size, no matter what the window shape or noise model; (2) the optimum window size, that is, the window size that minimizes both the bias error and the standard deviation of the centroid

estimate, is a function of the SNR and the noise model; (3) the optimum window shape is a function of the noise model; and (4) the subpixel bias error tends toward the sawtooth shape associated with the systematic truncation error when the noise is proportional to the signal. For both noise models, the rms value of the bias error increases at a slower rate for the Gaussian-shaped window than for the uniform window. However, the magnitude of this error is greater for the Gaussian-shaped window than for the uniform window when the noise is proportional to the square root of the signal amplitude; the error magnitude for the Gaussian-shaped window is less than that for the uniform window when the pixel-to-pixel noise is independent and mean zero Gaussian. It follows from this that in order to determine an optimum window size (and shape) for point target tracking, the SNR and noise process must be known.

Experimental Results

Experiments were run to verify the results predicted by simulation. A single camera was mounted directly over an LED target. The target was moved over ±0.05 in. in the object plane in 0.0025-in. steps using a computer-controlled linear stage and imaged with the camera (fig. 14). The displacement of the stage was measured using a laser interferometer to approximately 0.0001 in. Since the magnification factor for the camera was approximately 0.1, it was possible to resolve the displacement of the target in the image plane to better than 1/20 of a pixel. The centroid of the projected target image was calculated as the average of the centroid estimates obtained for 100 target images acquired at each location of the stage. A straight line was fit through the average centroid estimates as a function of the measured stage position. The bias error was then determined to be the difference between the straight-line fit and the average centroid estimate at each location.

Figures 15(a) and 15(b) show the bias errors for a uniform window and a Gaussian-shaped window. In figure 15(a) (for the uniform window), the larger amplitude error corresponds to $N = 4$ and the smaller amplitude error corresponds to $N = 6$. In figure 15(b) (for the Gaussian-shaped window), the larger amplitude error corresponds to $N = 5$ and the smaller amplitude error corresponds to $N = 15$. The image distribution for which the centroid was estimated is that shown in figure 16 and was the same for all N. Assuming a point target, the half-width of the distribution shown in figure 16 corresponds to $b \approx 6.0$. The jitter that is apparent in the data is the result of the noise model and the thresholding technique discussed previously.

In order to determine the relationship between the signal SNR, window size and shape, and accuracy, the experiment described above was repeated for different sensor integration times. Figure 17 presents the rms values of the bias error (over 9 cycles) for different SNR's and window widths. Figure 17(a) shows the results obtained with a uniform window, and figure 17(b) shows the results obtained with a Gaussian-shaped window.

In addition to the bias error, the standard deviation of the centroid estimate at a single position of the stage was measured. These results are shown in figure 18. As expected, the standard deviation of the centroid estimate increases with increasing window size. The increase in the standard deviation again at small window sizes is believed to result from thresholding. As the window size decreases to the point where the signal is truncated, those pixels at either edge of the window have greater noise associated with them. When the threshold is set as the average of the signals from these two pixels and subtracted from the signal at each pixel within the window, the random error in the estimate of the centroid is increased. Therefore, the variation from sample to sample increases.

From the above results, the uniform window shape is optimum for centroid estimation in the optical tracking system. Furthermore, $N/b \approx 1.5$ is the optimum ratio of window width to width of the target image distribution for SNR's from about 50 to 100. This ratio of window size to distribution width provides the minimum total error, where the total error is the sum of the rms value of the bias error and the standard deviation of the centroid estimate.

Centroid-Estimation Algorithm

A flowchart of the centroid-estimation algorithm is shown in figure 19. The subpixel centroid estimate is calculated in the following way. During tracking, a search is made for the peak pixel location of each target prior to computation of the centroid. The pixel location of peak light intensity is stored and used to set up a window of 81 pixels centered about the peak. Each pixel has a slightly different response, that is, a slightly different gain and zero point. Prior to computation of the centroid, the values of light intensity are corrected for pixel nonuniform responsivity and the background light level is subtracted for pixels falling within the window. A second coarse search for the peak intensity is then performed over the corrected light intensity values.

Before the centroid is estimated, the width of the distribution is determined by computing the second

moment of the target image distribution. The second moment is calculated as

$$\bar{\sigma} = \frac{\sum_{n=x_p-15}^{x_p+15} n^2 I(n)}{\sum_{n=x_p-15}^{x_p+15} I(n)} - \bar{x}^2$$

where $\bar{x}$ is the centroid of the distribution calculated over ± 15 pixels centered about the peak, $I(n)$ is the digital value of the light intensity for pixel n, and x_p is the pixel location of the peak signal.

The value of N used in the centroid calculation is equal to the nearest integer value of the second moment $\bar{\sigma}$ plus one pixel. The subpixel centroid estimate is calculated as

$$\bar{x}_{sw} = \frac{\sum_{n=x_p-N}^{x_p+N} nI(n)}{\sum_{n=x_p-N}^{x_p+N} I(n)}$$

Figure 20 shows the subpixel bias error from the use of the centroid-estimation algorithm that adjusts the window size; the window shape is uniform. Figure 21 shows the standard deviations of the centroid estimate for a uniform window of variable width and a uniform window with a fixed width of $N = 14$. The value of $N = 14$ was chosen as the size required to minimize the systematic error for the maximum signal obtained during tracking with the OMS. The maximum signal has an SNR of approximately 200. Adjusting the window size to match the width of the distribution minimizes the systematic error as well as the standard deviation of the centroid estimate over a wider range of SNR's than does using a window of fixed size.

Conclusions

The effects of window size and shape on the accuracy of subpixel centroid estimation have been presented. Two different noise models and window shapes have been studied. The shapes include a uniform window and a Gaussian-shaped window. The noise models studied include random mean zero Gaussian, independent pixel to pixel and independent of signal amplitude, and noise proportional to the square root of the signal amplitude.

Fourier analysis has been used to determine the form and magnitude of the systematic error due to windowing. It has been shown that the form of the subpixel error due to windowing resembles one period of a sawtooth compared with the pure sinusoidal waveform that is obtained when the signal is undersampled. Furthermore, it has been shown that the magnitude of this systematic error is smaller for a Gaussian-shaped window than for a uniform window.

Simulations have been run to explore the sensitivity of the centroid-estimation algorithm to window size and shape in the presence of noise and to determine the window shape and size that minimize the error. Experiments have been conducted to verify the behavior predicted by simulation. The results of the simulations and experiments revealed the following: (1) for noise that is proportional to the square root of the signal amplitude, the optimum window shape is uniform, and for noise that is independent of signal amplitude, with a low ratio of peak signal to standard deviation of background signal (SNR), the optimum window shape is Gaussian; and (2) matching the size of the window to the width of the target image distribution improves the accuracy of the centroid estimate for both noise models and both window shapes. The optimum ratio of window width to width of the target distribution is approximately 1.5 for the uniform window and noise proportional to signal amplitude.

The results of the analysis have been used to develop a new centroid-estimation algorithm that increases the accuracy of subpixel centroid estimation of (nearly) point target images when the noise is proportional to signal amplitude and the signal amplitude and shape vary from frame to frame. In the algorithm, the width of the data window is matched to the estimated width of the image distribution. Calculating the centroid over a window that is matched in size to the width of the distribution yields a subpixel centroid estimate with smaller total error over a wider range of SNR's than that from a calculation with a window of fixed size. This improvement in centroid estimation has been developed for a point target tracking system in order to increase the dynamic range of the system.

NASA Langley Research Center
Hampton, VA 23681-0001
June 22, 1993

References

1. Armstrong, R. W.; and Staley, Douglas A.: A Survey of Current Solid State Star Tracker Technology. *J. Astronaut. Sci.*, vol. 33, no. 4, Oct.–Dec. 1985, pp. 341–352.

2. Bales, John W.; and Barker, L. Keith: *Marking Parts To Aid Robot Vision.* NASA TP-1819, 1981.

3. El-Hakim, S. F.: Real-Time Image Metrology With CCD Cameras. *Photogramm. Eng. & Remote Sens.*, vol. 52, no. 11, Nov. 1986, pp. 1757–1766.

4. Grossman, S. B.; and Emmons, R. B.: Performance Analysis and Size Optimization of Focal Planes for Point Source Tracking Algorithm Applications. *Focal Plane Methodologies III*, Volume 350 of SPIE Proceedings, J. T. Hall and W. S. Chan, eds., International Soc. for Optical Engineering, 1983, pp. 94–108.

5. Stanton, Richard H.; Alexander, James W.; Dennison, Edwin W.; Glavich, Thomas A.; and Hovland, Larry F.: Optical Tracking Using Charge-Coupled Devices. *Opt. Eng.*, vol. 26, no. 9, Sept. 1987, pp. 930–938.

6. Cox, J. Allen: Advantages of Hexagonal Detectors and Variable Focus for Point-Source Sensors. *Opt. Eng.*, vol. 28, no. 11, Nov. 1989, pp. 1145–1150.

7. Alexander, Brian F.; and Ng, Kim Chew: Elimination of Systematic Error in Subpixel Accuracy Centroid Estimation. *Opt. Eng.*, vol. 30, no. 9, Sept. 1991, pp. 1320–1331.

8. Wittenstein, W.; Fontanella, J. C.; Newbery, A. R.; and Baars, J.: The Definition of the OTF and the Measurement of Aliasing for Sampled Imaging Systems. *Opt. Acta*, vol. 29, no. 1, 1982, pp. 41–50.

9. Park, Stephen K.; and Schowengerdt, Robert A.: Image Sampling, Reconstruction, and the Effect of Sample-Scene Phasing. *Appl. Opt.*, vol. 21, no. 17, Sept. 1, 1982, pp. 3142–3151.

10. Park, S. K.; Kaczynski, M.-A.; and Schowengerdt, R. A.: Modulation-Transfer-Function Analysis for Sampled Image Systems. *Appl. Opt.*, vol. 23, no. 15, Aug. 1, 1984, pp. 2572–2582.

11. Gaskill, Jack D.: *Linear Systems, Fourier Transforms, and Optics.* John Wiley & Sons, Inc., c.1978.

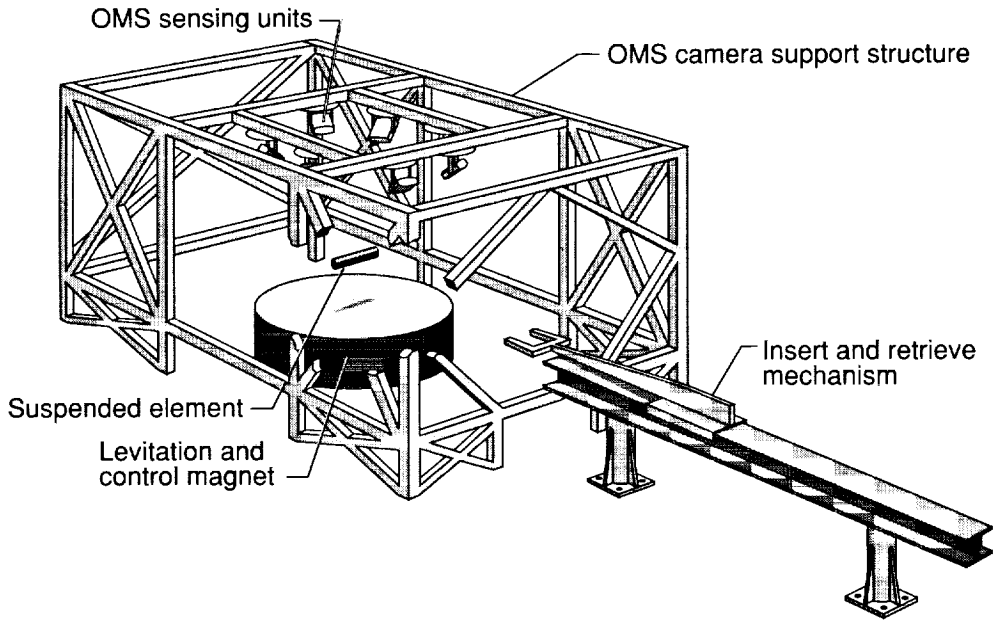

Figure 1. Optical measurement system (OMS) of large gap magnetic suspension system (LGMSS).

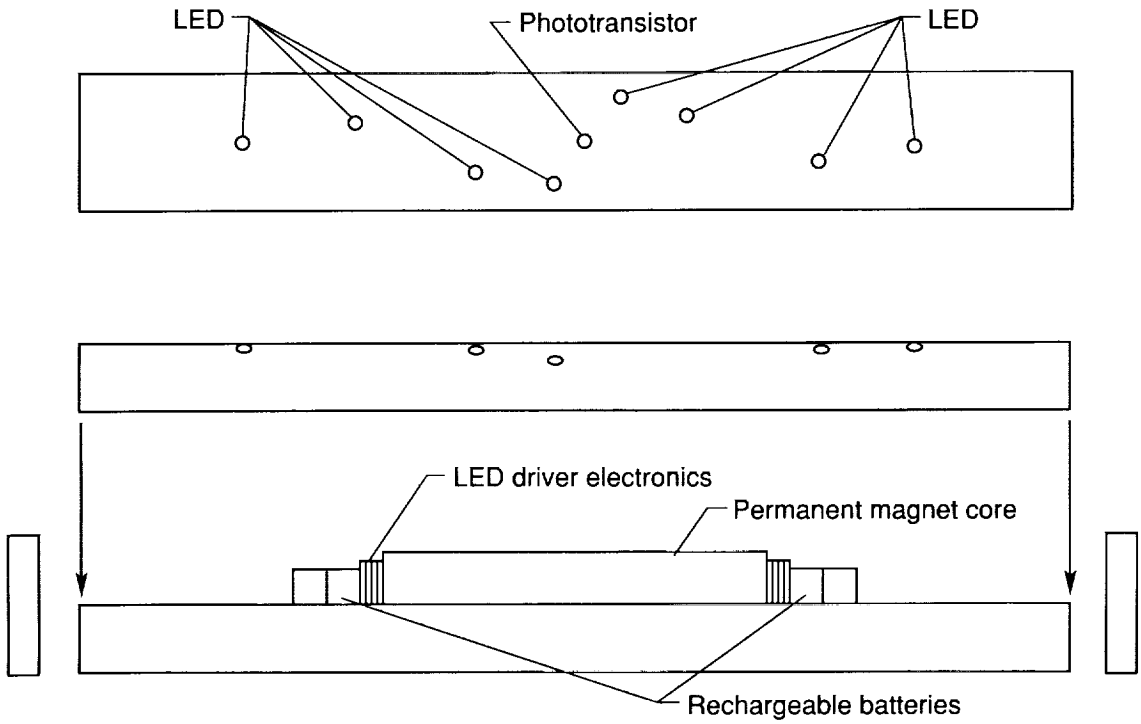

Figure 2. Levitated cylinder with locations of eight LED targets.

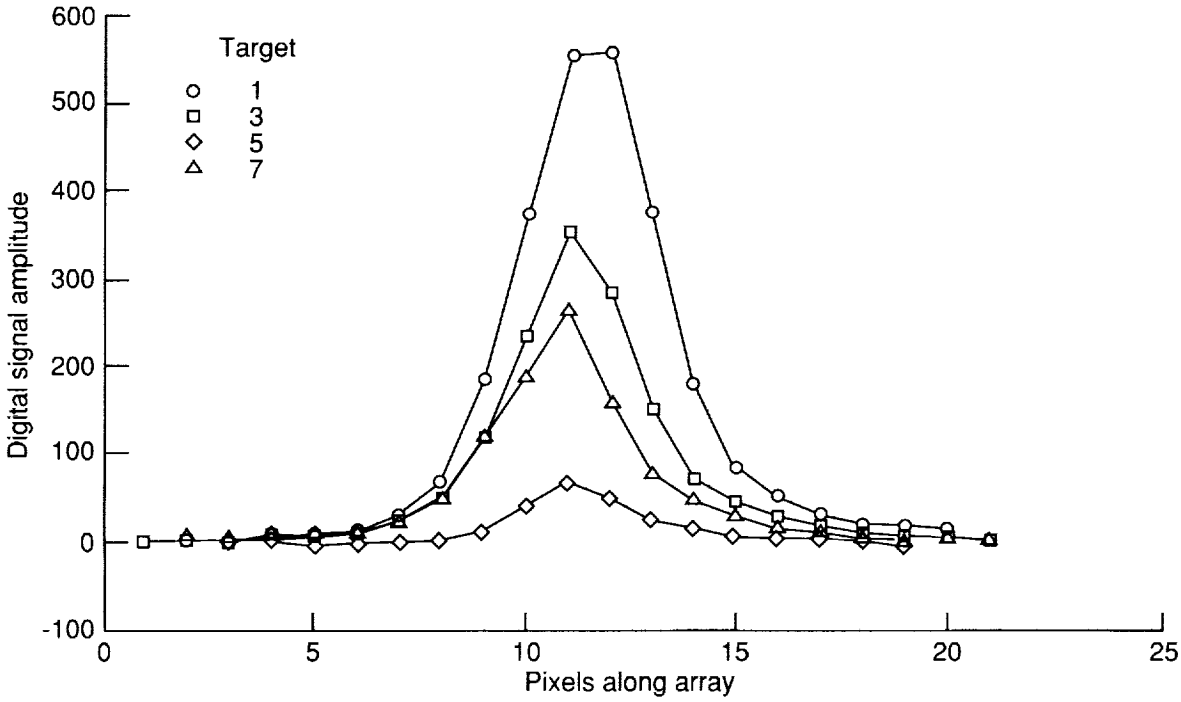

Figure 3. Digital signals (expanded) corresponding to light intensity distributions for images of targets 1, 3, 5, and 7 as viewed from sensor 7 in OMS. All images have been referenced to same peak pixel location to better illustrate range of sizes and shapes of sampled image distributions that can be generated by different targets.

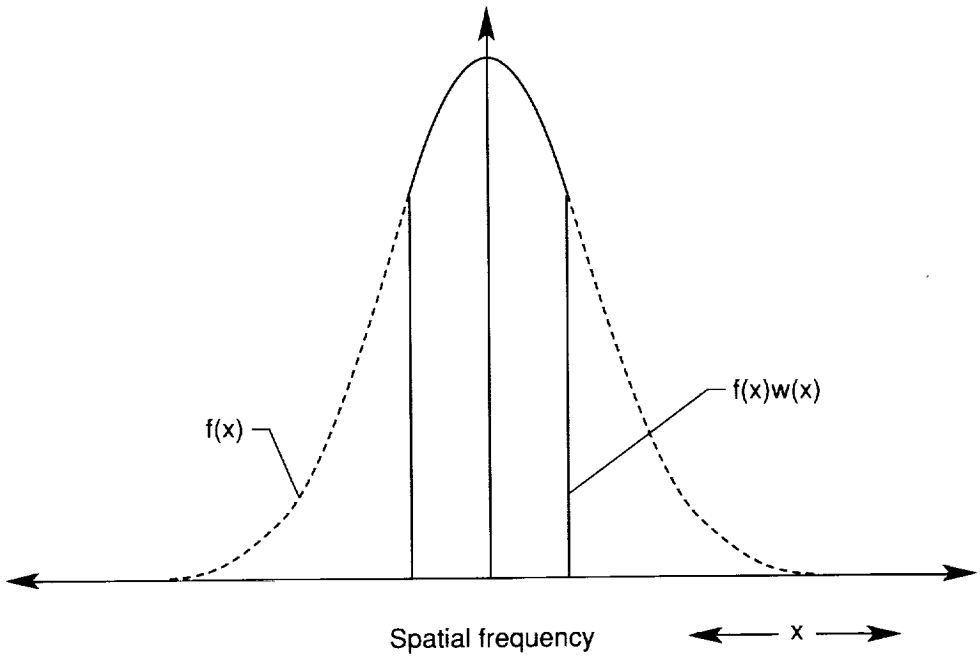

(a) Continuous distribution $f(x)$.

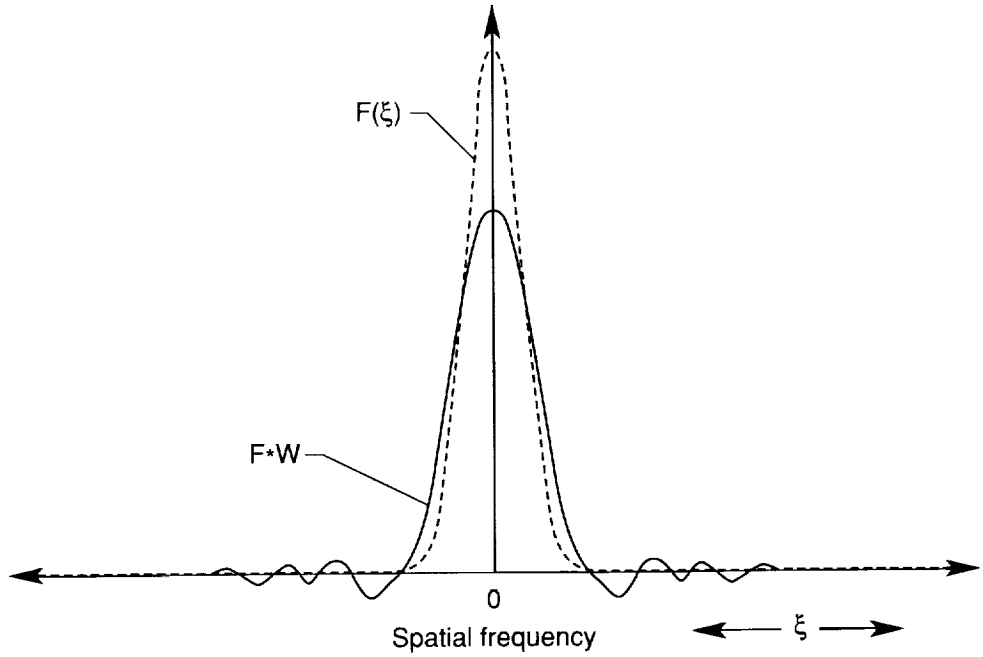

(b) Fourier transform of $f(x)$ multiplied by Fourier transform of window function $w(x)$, uniform window placed symmetrically about $f(x)$.

Figure 4. Effect of windowing.

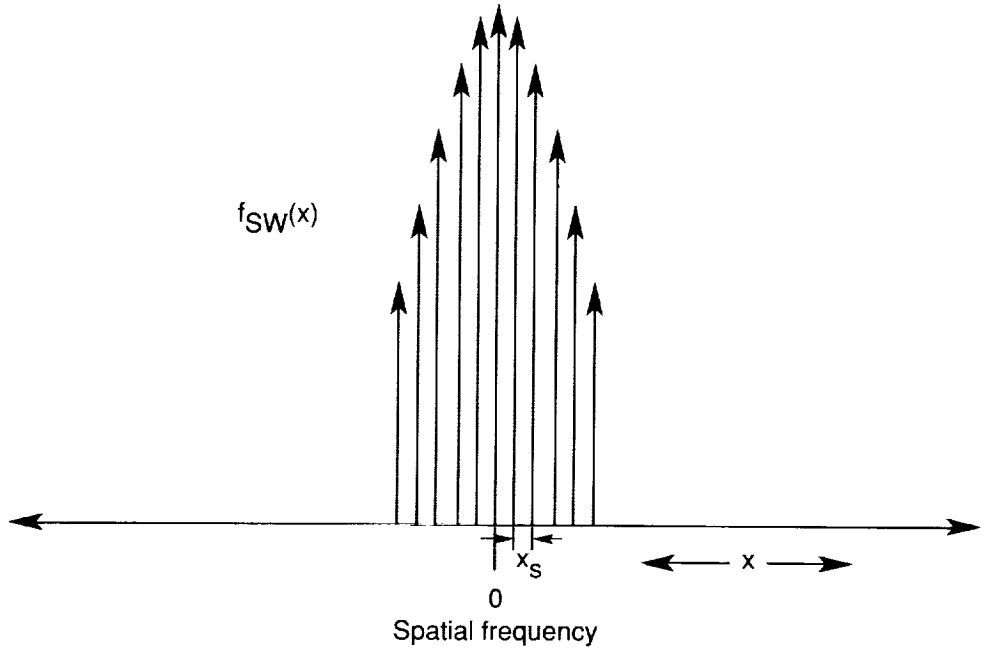

(a) Representative signal.

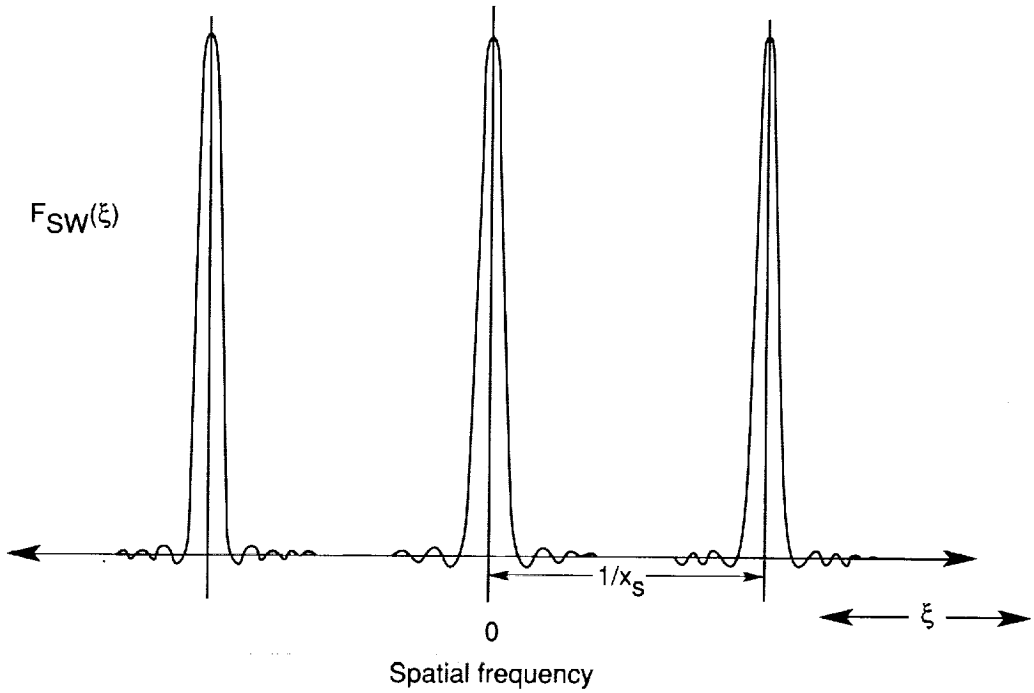

(b) Fourier transform of signal.

Figure 5. Representative sampled and windowed signal corresponding to point target image and Fourier transform of this signal.

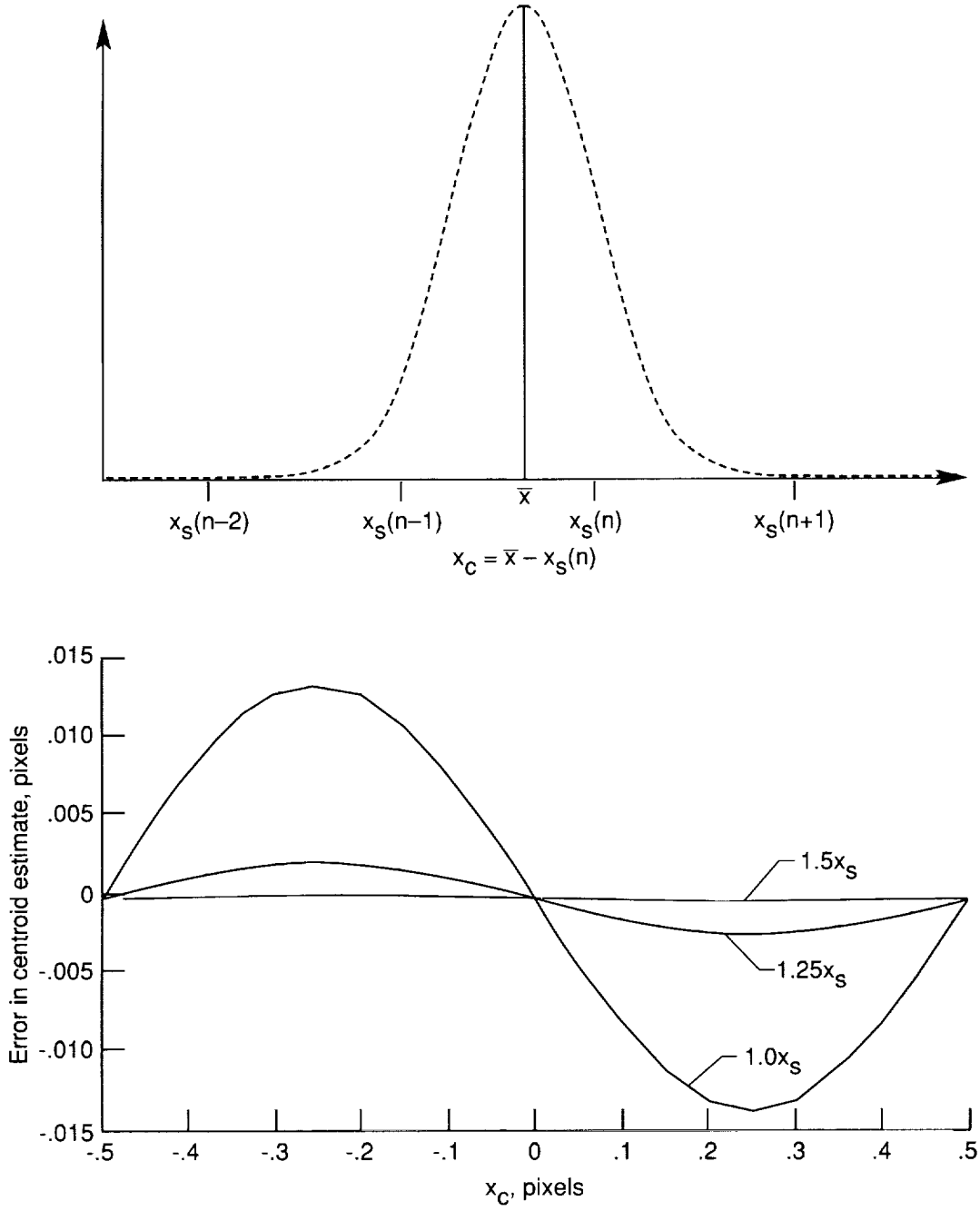

Figure 6. Error in centroid estimate as function of x_c generated from simulated data. Target was assumed to be point source, PSF was assumed to be Gaussian with widths ranging from 1.0 to 1.5 times sample spacing x_s, and pixel response function was assumed to be uniform and equal in width to sample spacing.

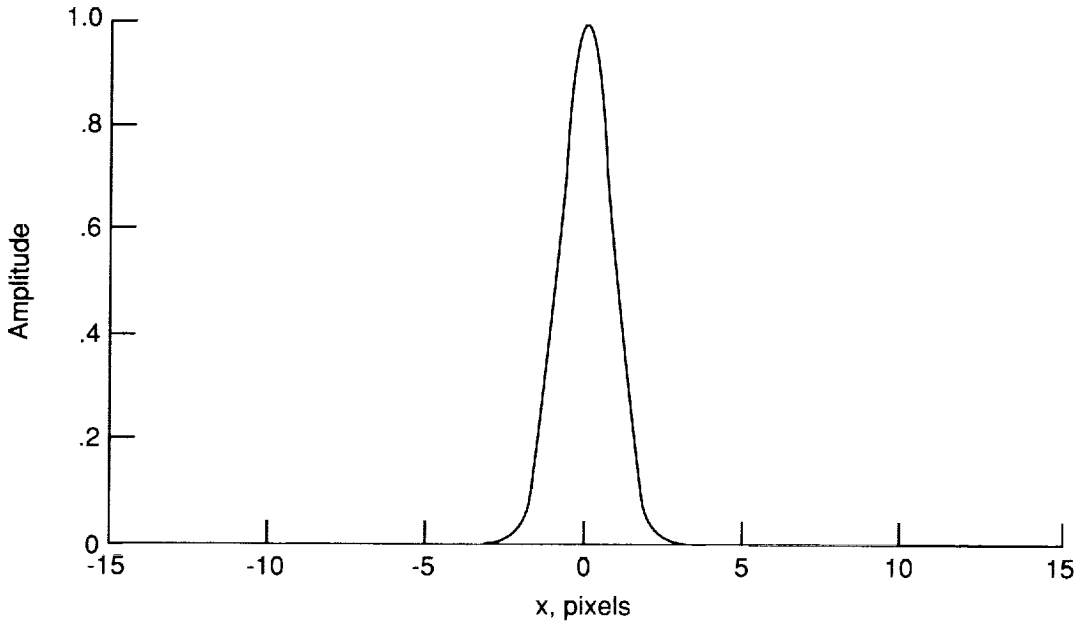

(a) Simulated PSF; $b = 1.0$.

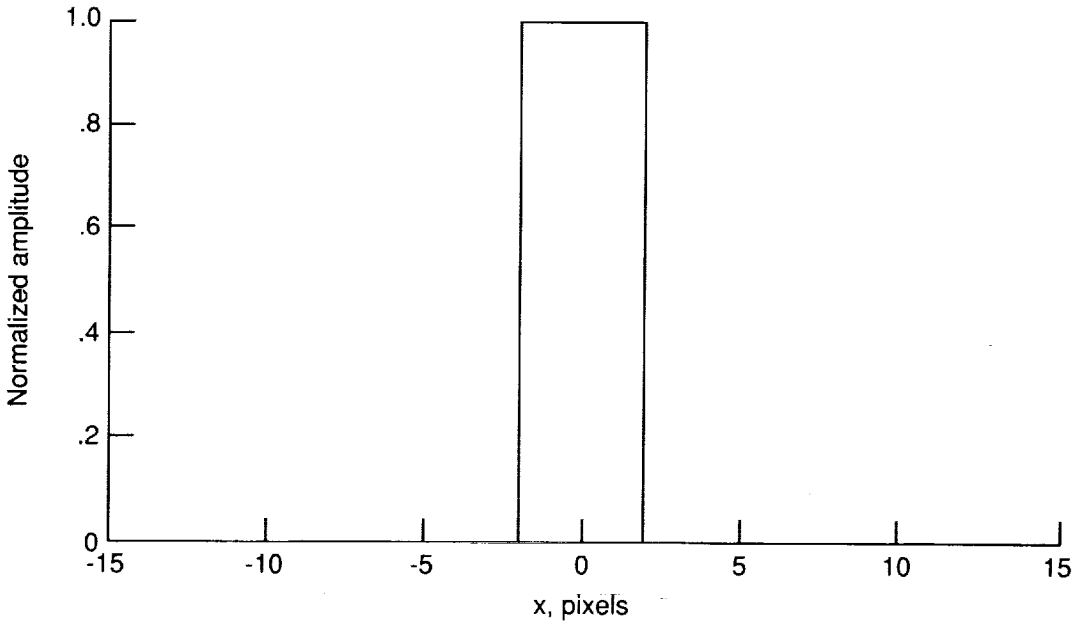

(b) Simulated target of uniform intensity and width of $4x_s$.

Figure 7. Simulated digital data for different target widths and corresponding Fourier transforms.

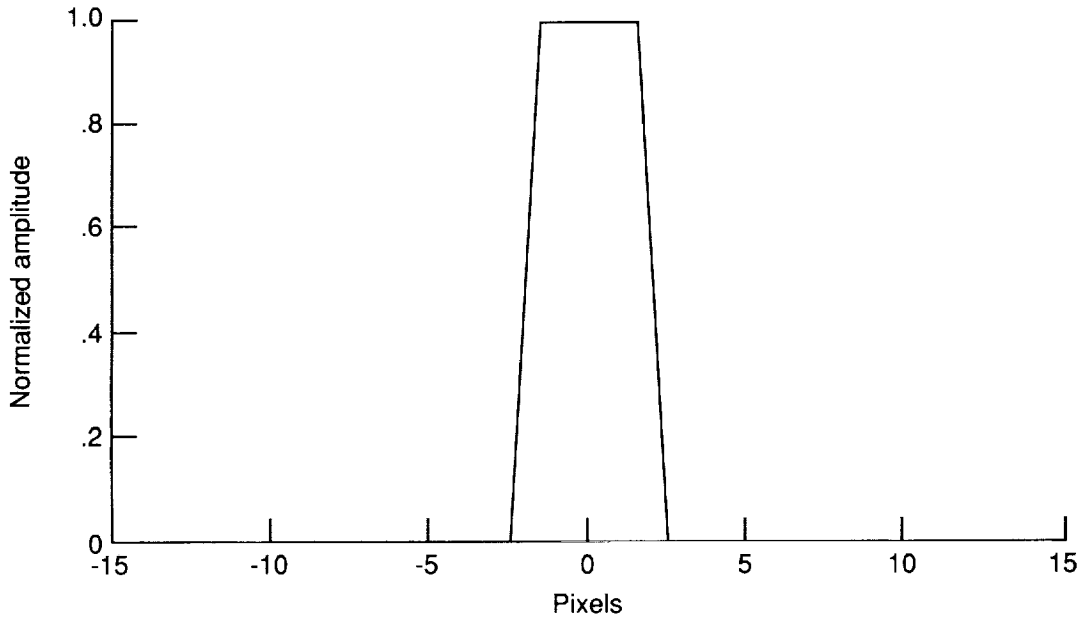

(c) Convolution of target from figure 7(b) with $r(x)$ of width x_s.

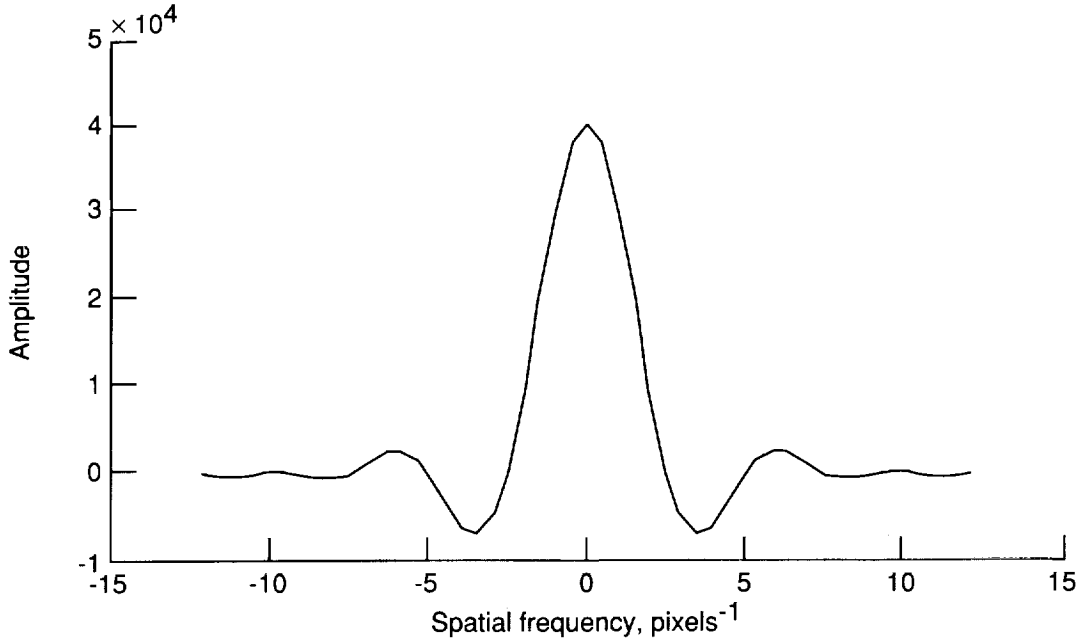

(d) Fourier transform of convolution from figure 7(c).

Figure 7. Continued.

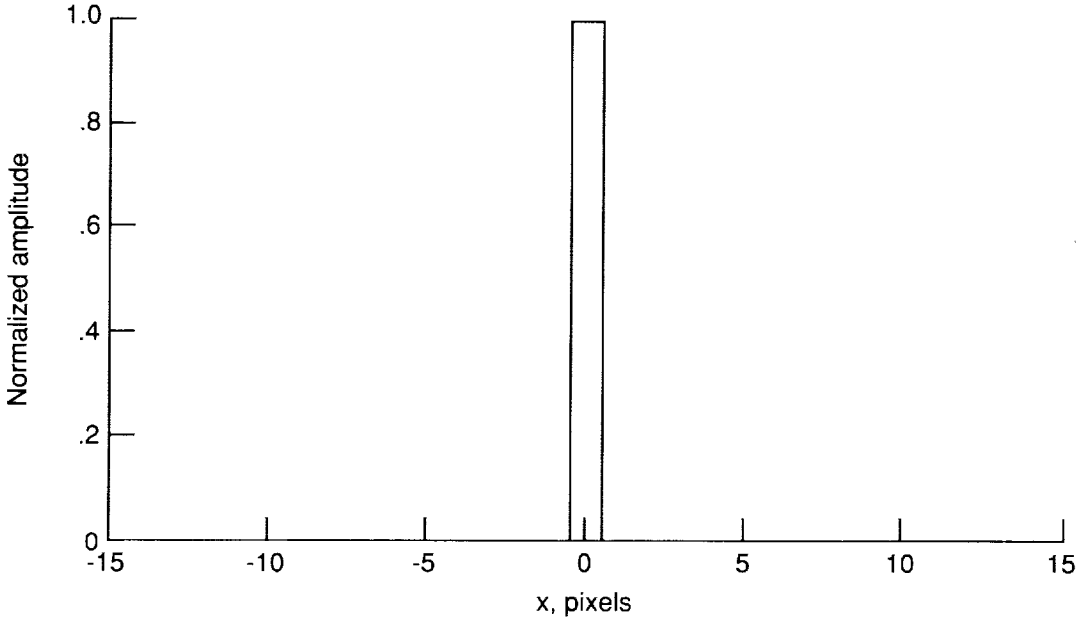

(e) Simulated target of uniform intensity and width of x_s.

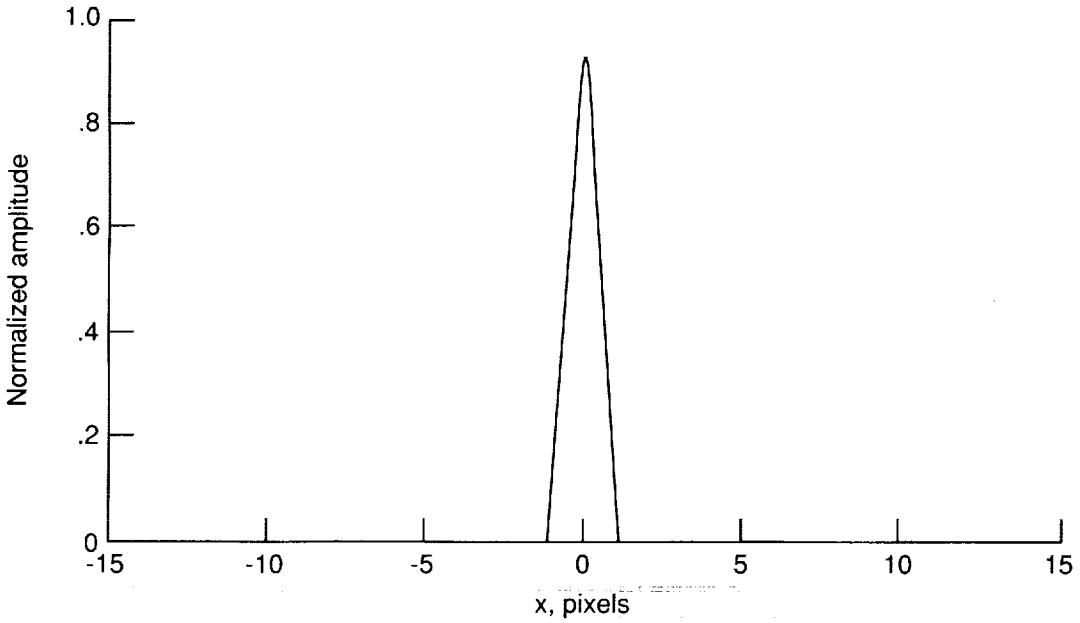

(f) Convolution of target from figure 7(e) with pixel response function of width x_s.

Figure 7. Continued.

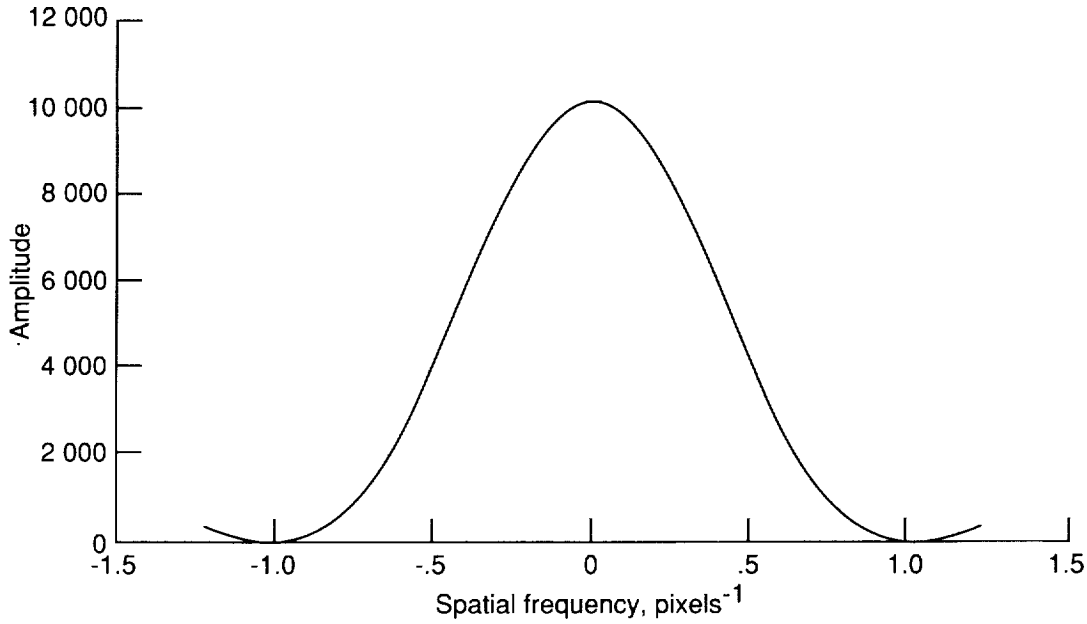

(g) Fourier transform of convolution from figure 7(f).

Figure 7. Concluded.

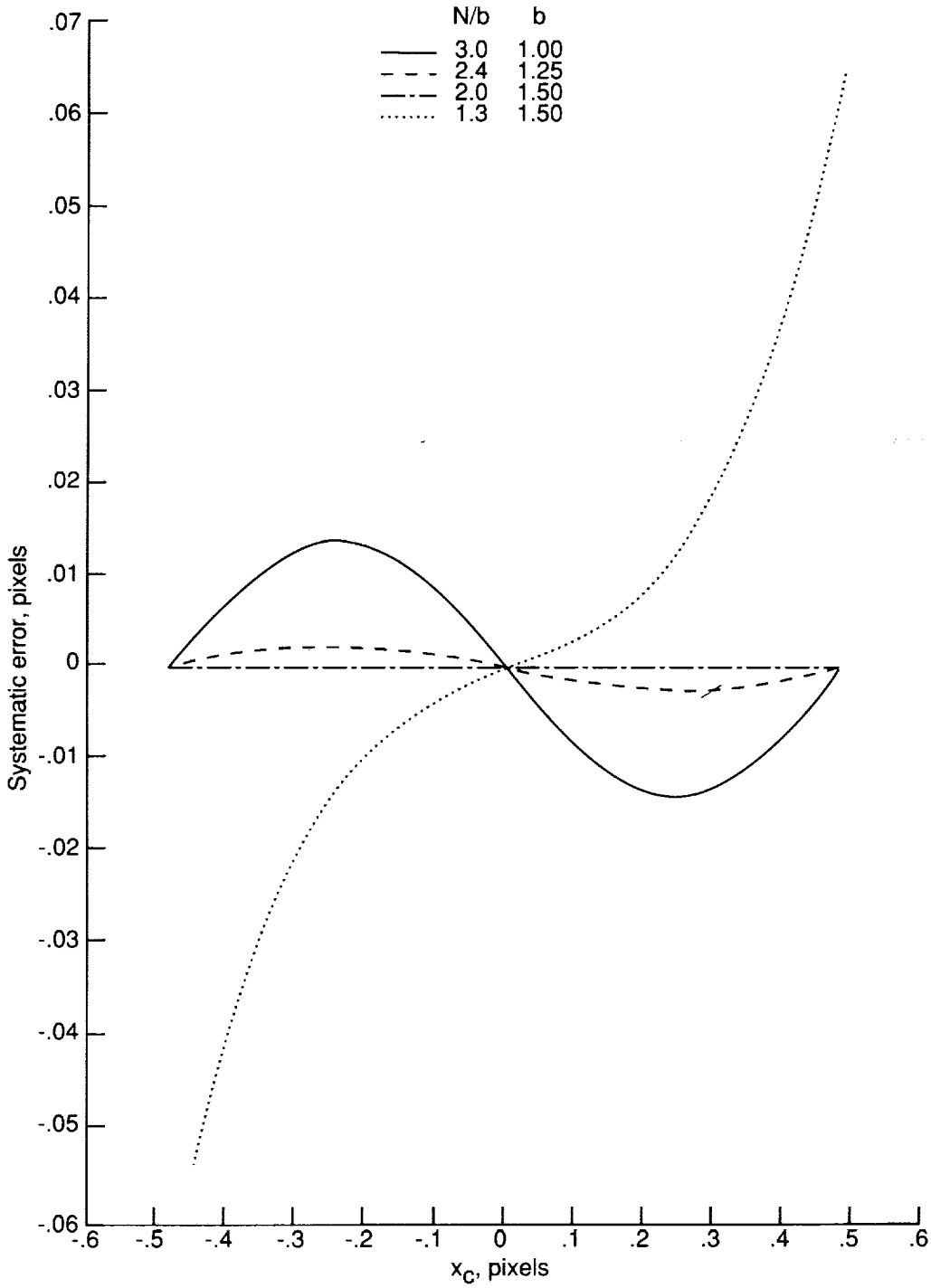

Figure 8. Four curves of subpixel error as function of x_c for uniform window.

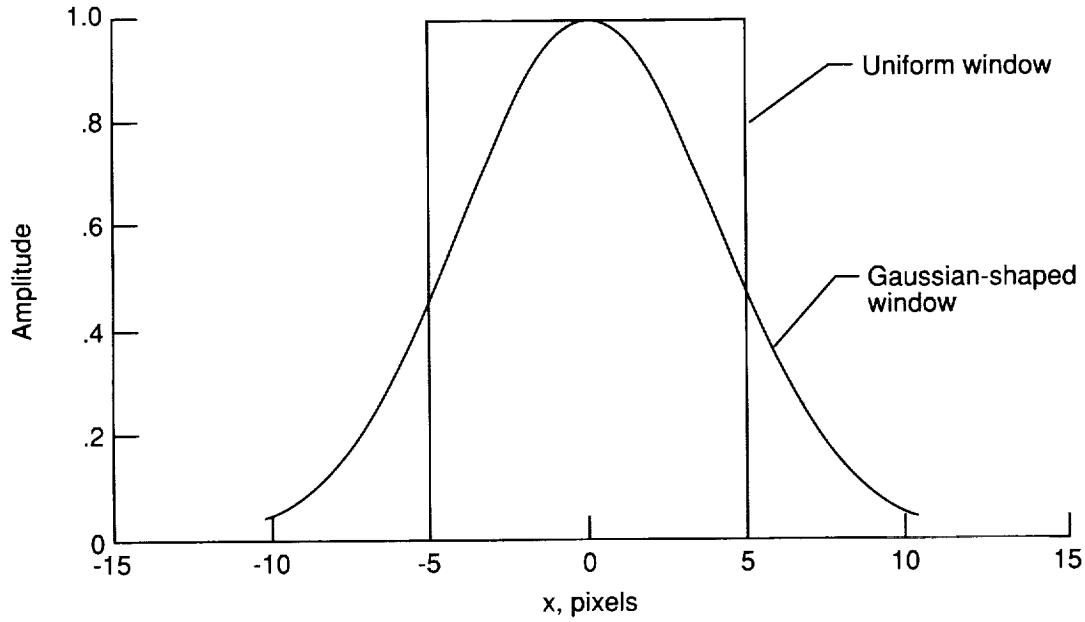

(a) $w(x)$.

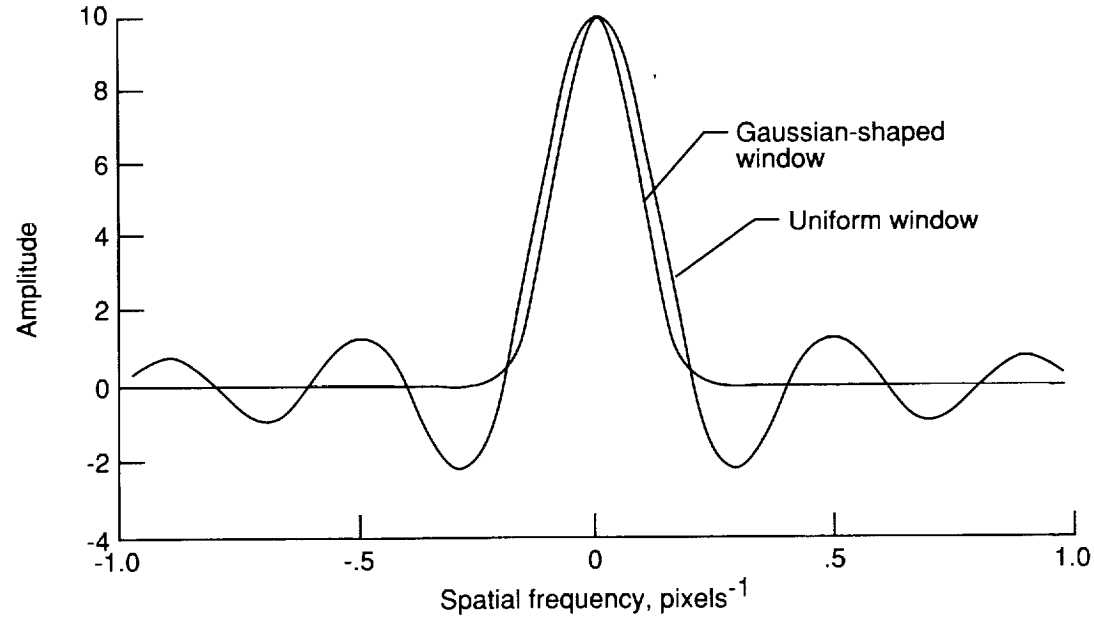

(b) $W(\xi)$.

Figure 9. Representative functions $w(x)$ and $W(\xi)$ for Gaussian-shaped window and uniform window. $N = 5$.

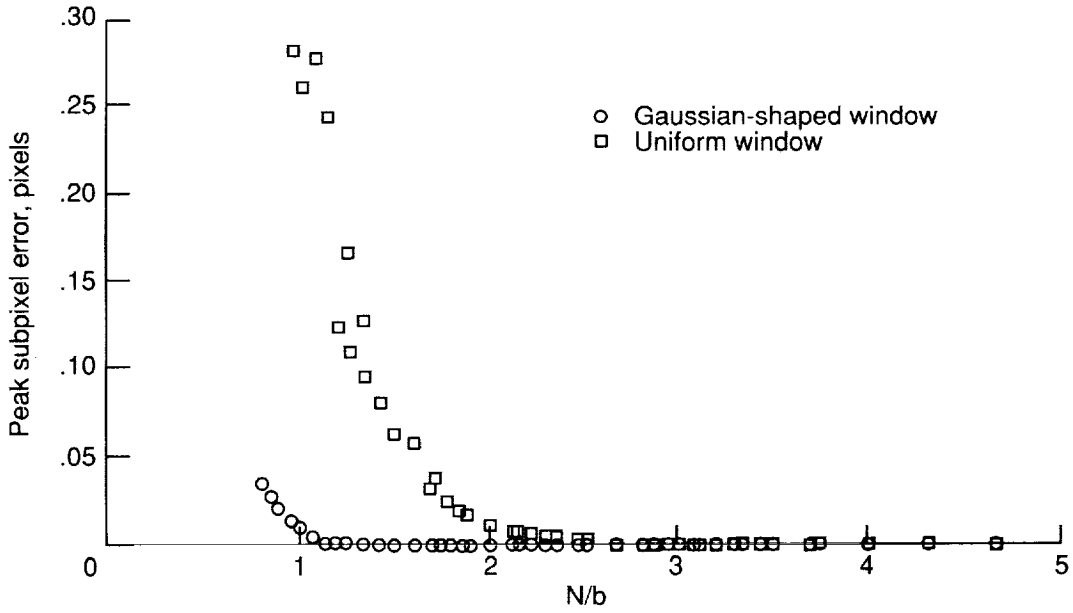

Figure 10. Peak subpixel error plotted as function of N/b for uniform window and Gaussian-shaped window.

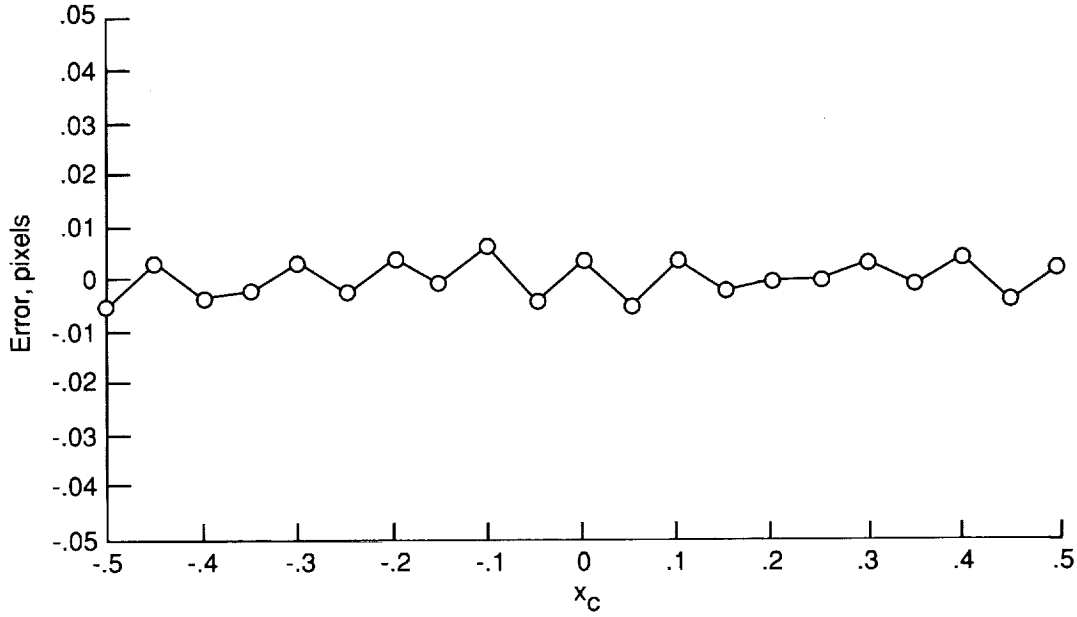

(a) Gaussian mean zero noise and uniform window; standard deviation, 0.01.

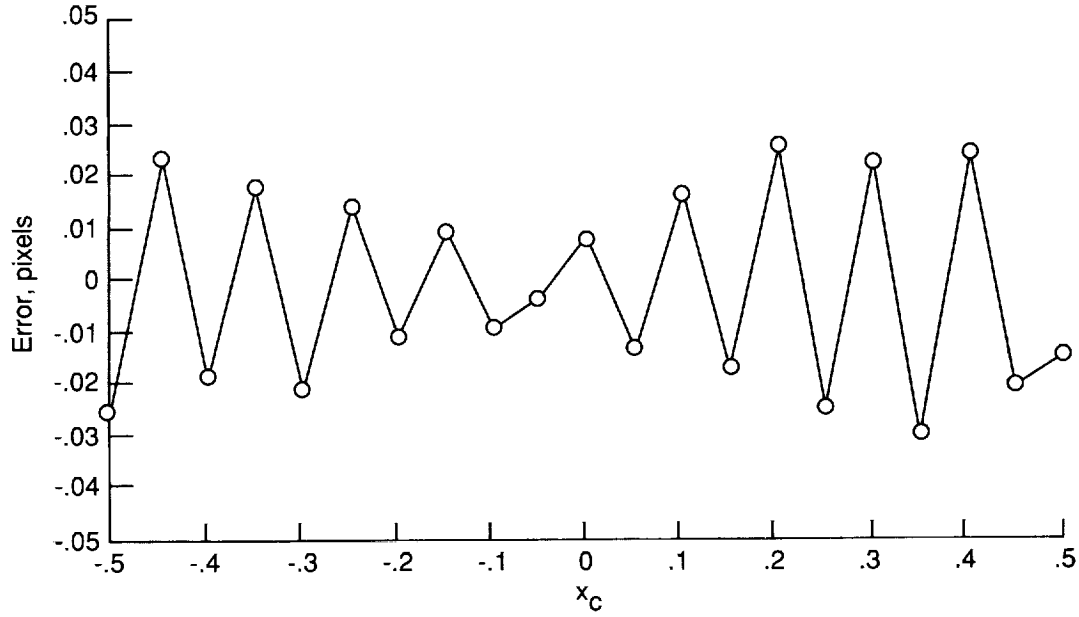

(b) Gaussian mean zero noise and Gaussian-shaped window; standard deviation, 0.01.

Figure 11. Average subpixel error as function of position x_c for combinations of noise model and window shape. $N/b = 2.105$.

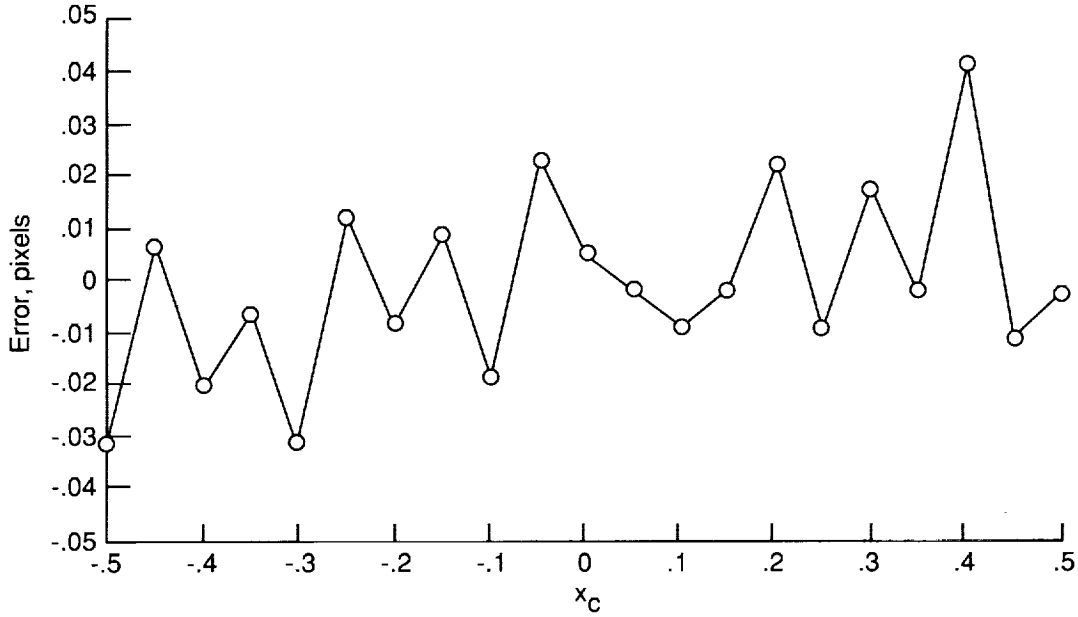

(c) Noise proportional to square root of signal amplitude and uniform window; standard deviation, 0.1.

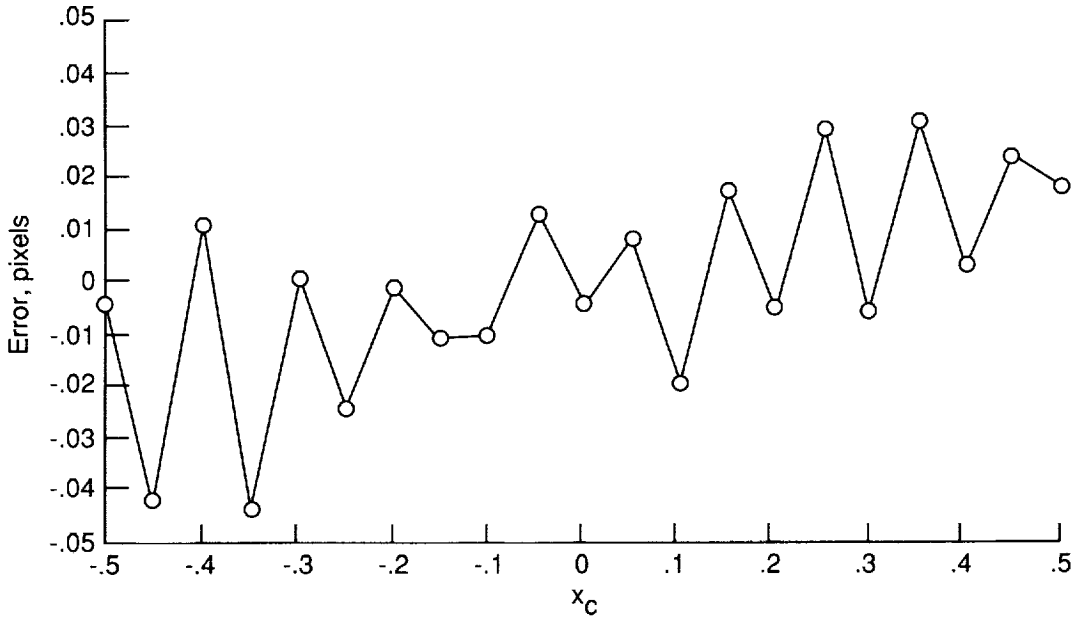

(d) Noise proportional to square root of signal amplitude and Gaussian-shaped window; standard deviation, 0.1.

Figure 11. Concluded.

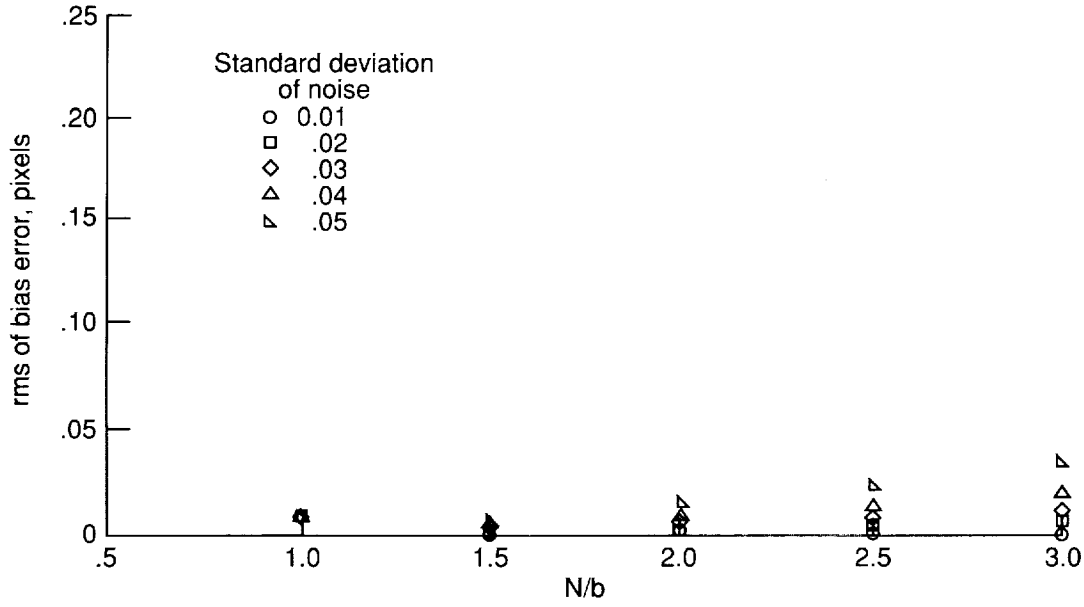

(a) Gaussian mean zero noise and uniform window.

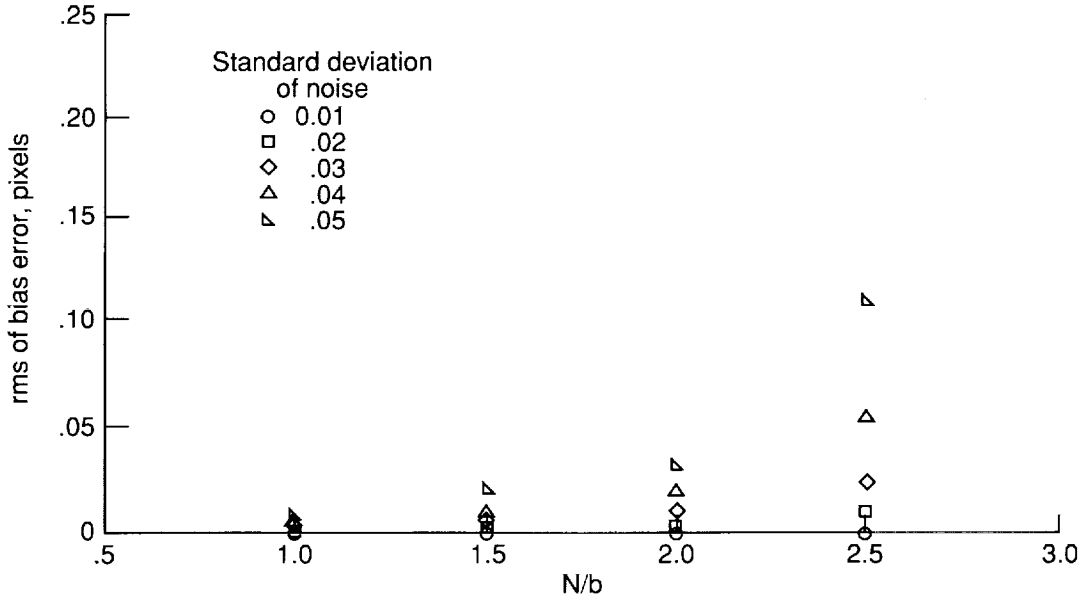

(b) Gaussian mean zero noise and Gaussian-shaped window.

Figure 12. Root-mean-square of bias error over single pixel.

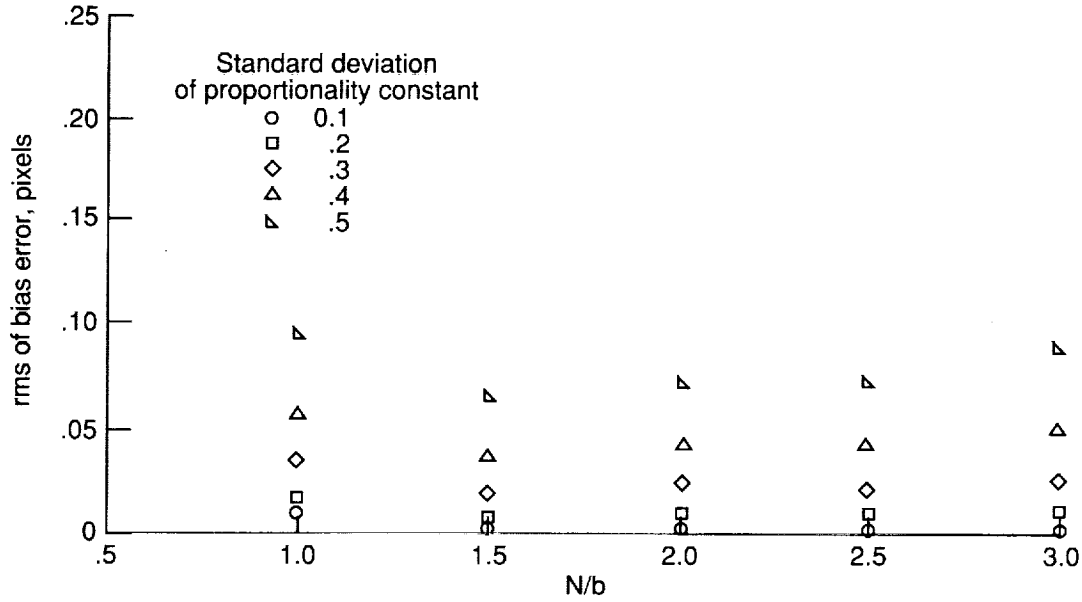

(c) Noise proportional to square root of signal amplitude and uniform window.

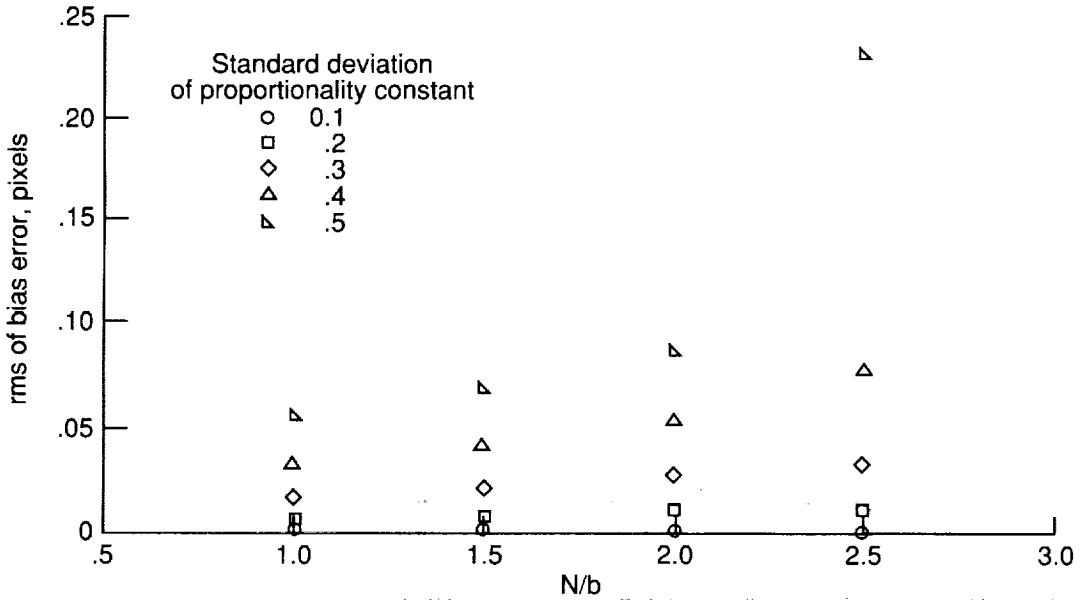

(d) Noise proportional to square root of signal amplitude and Gaussian-shaped window.

Figure 12. Concluded.

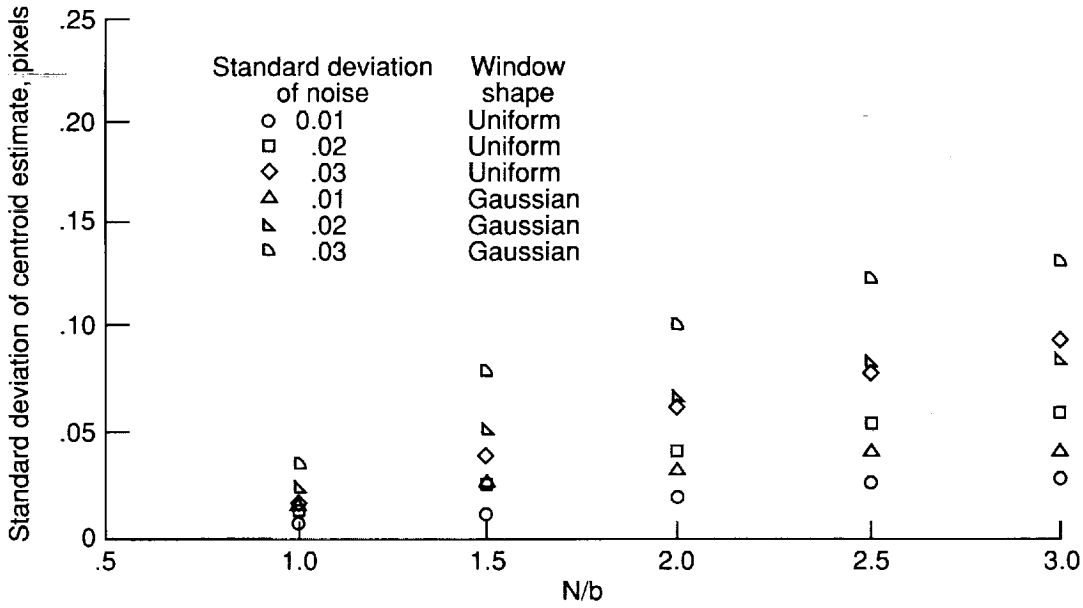

(a) Gaussian mean zero noise.

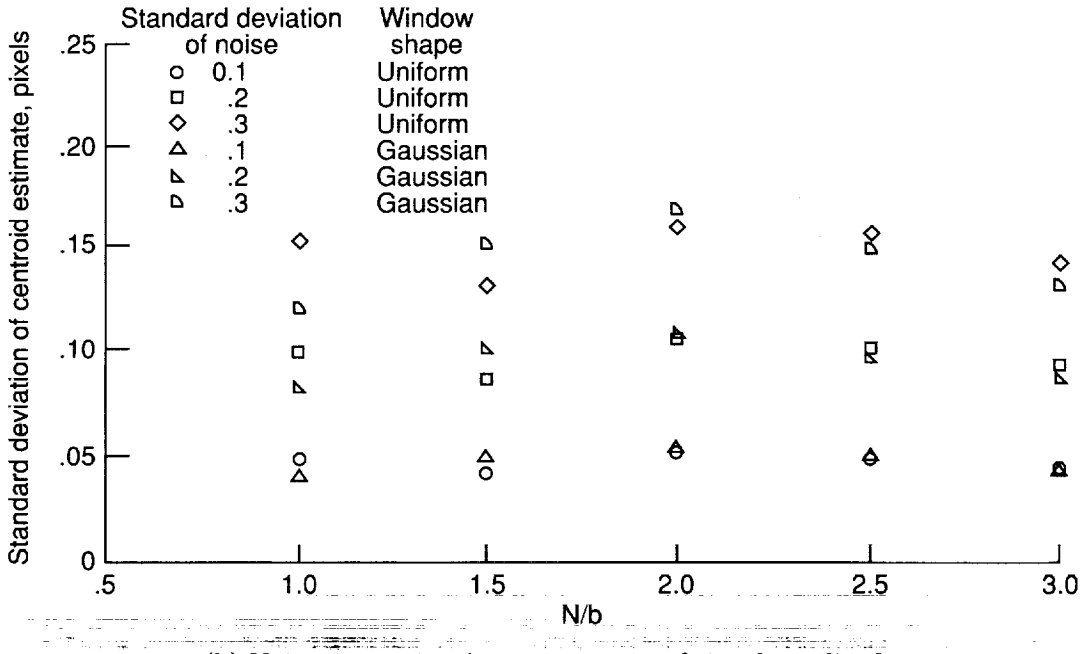

(b) Noise proportional to square root of signal amplitude.

Figure 13. Predicted standard deviations of centroid estimates at any single subpixel position.

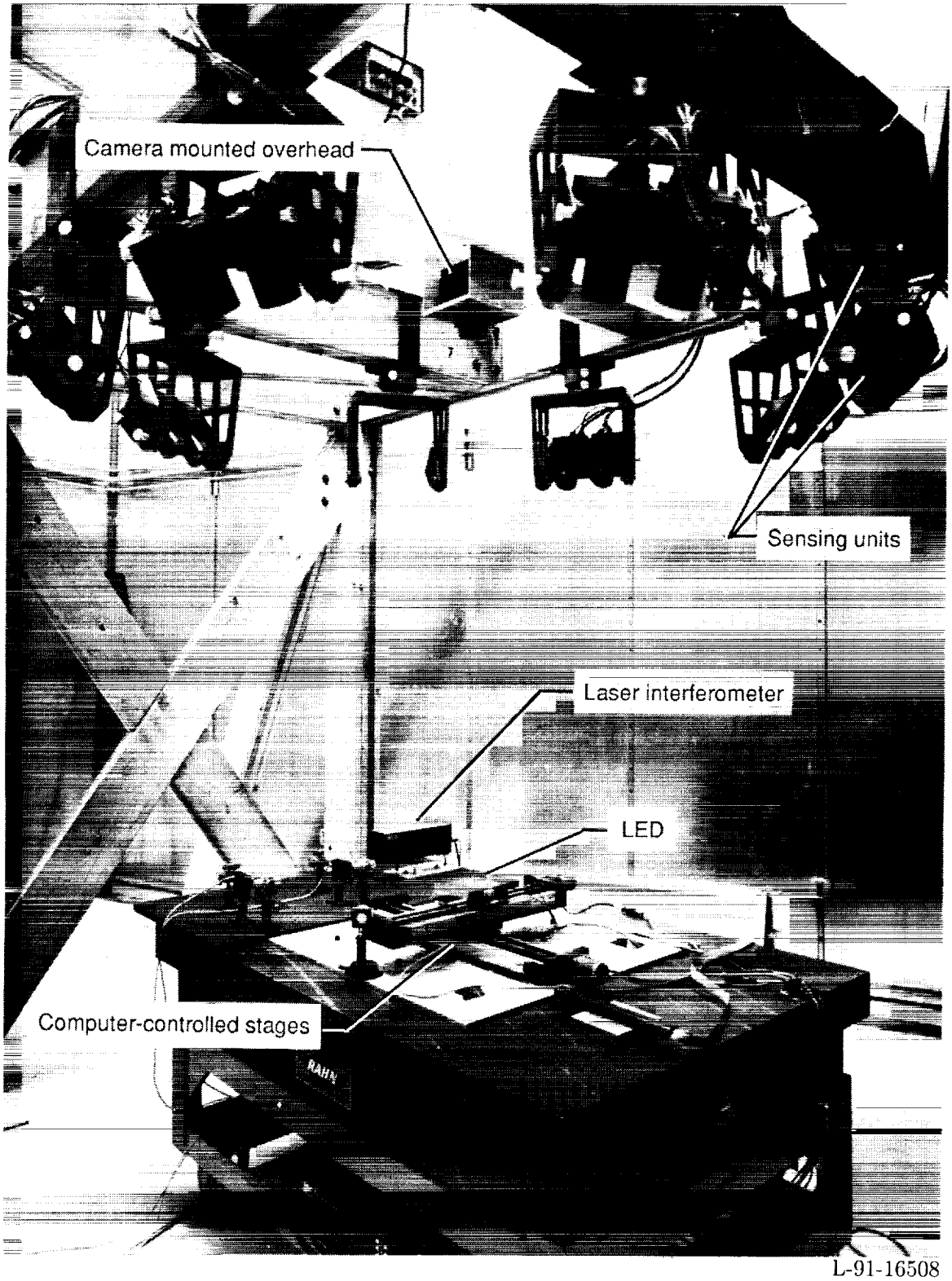

Figure 14. Experimental setup showing camera mounted overhead of diode and computer-controlled linear stages.

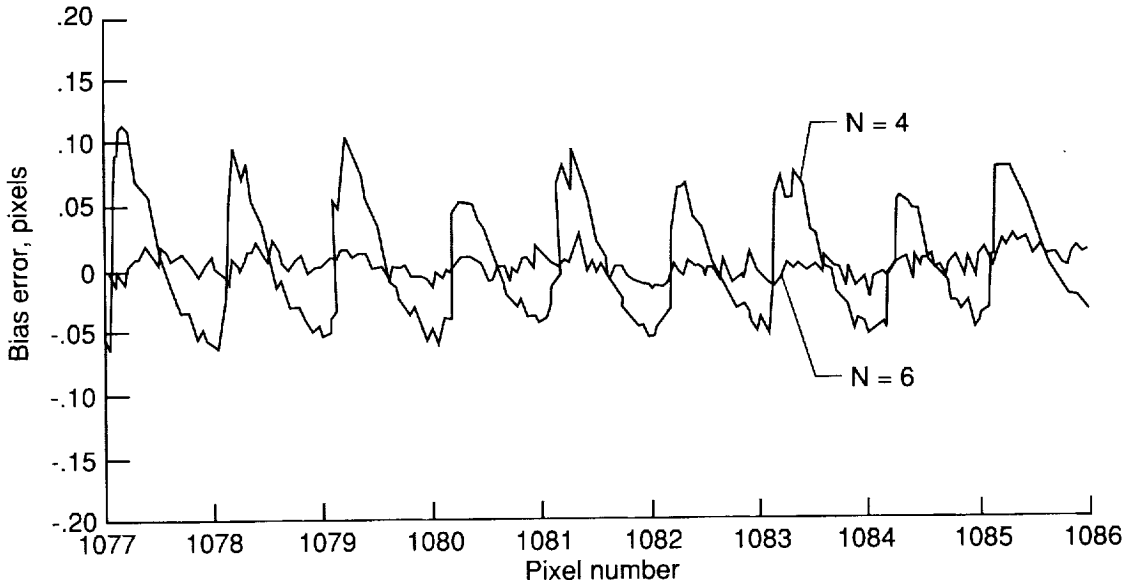

(a) Uniform window.

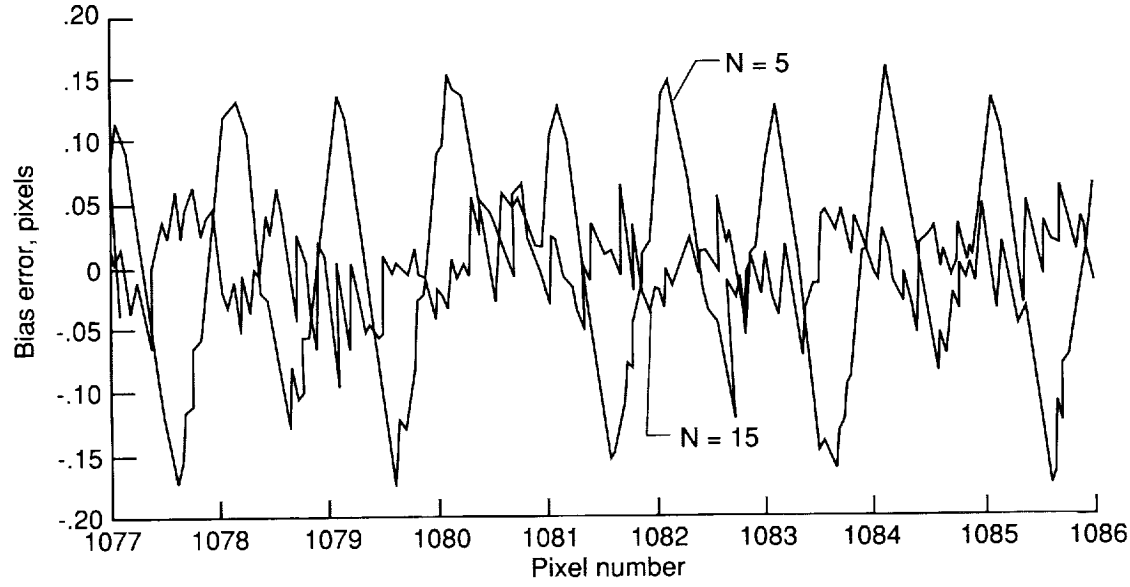

(b) Gaussian-shaped window.

Figure 15. Subpixel bias error for uniform and Gaussian-shaped windows.

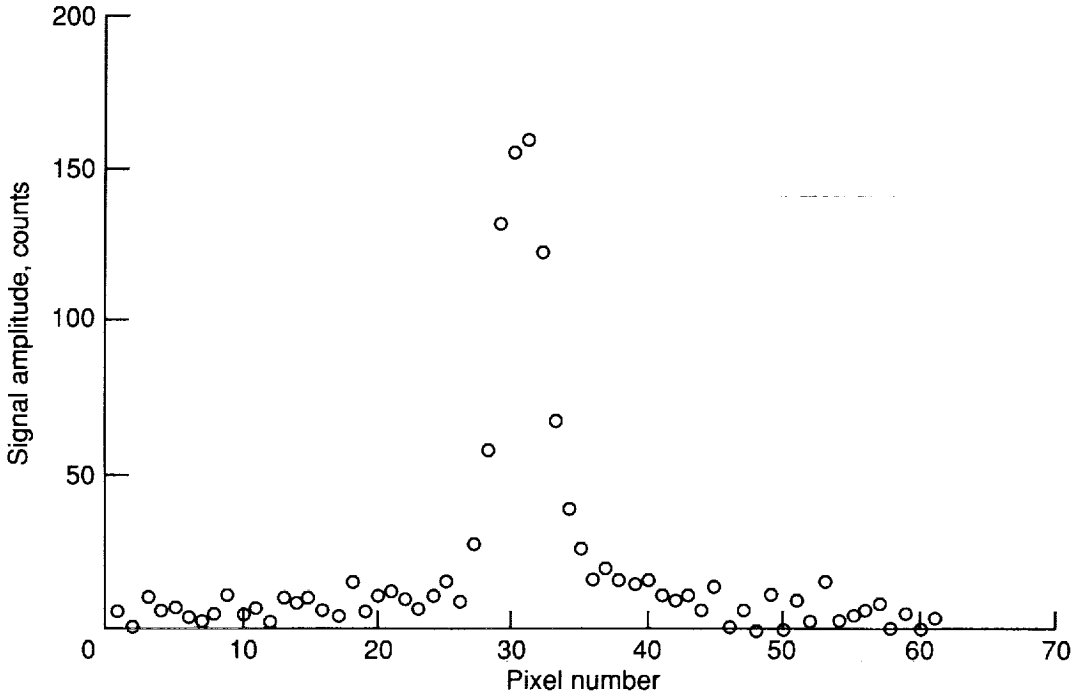

Figure 16. Representative target signal, at an integration time of 3 msec, that was used to generate results depicted in figure 15.

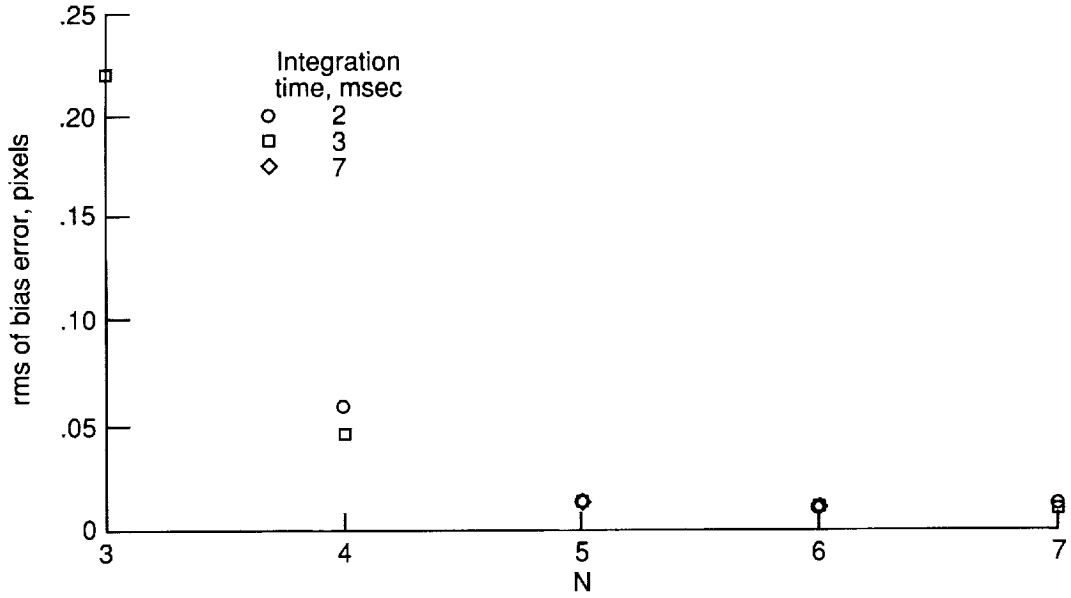

(a) Uniform window.

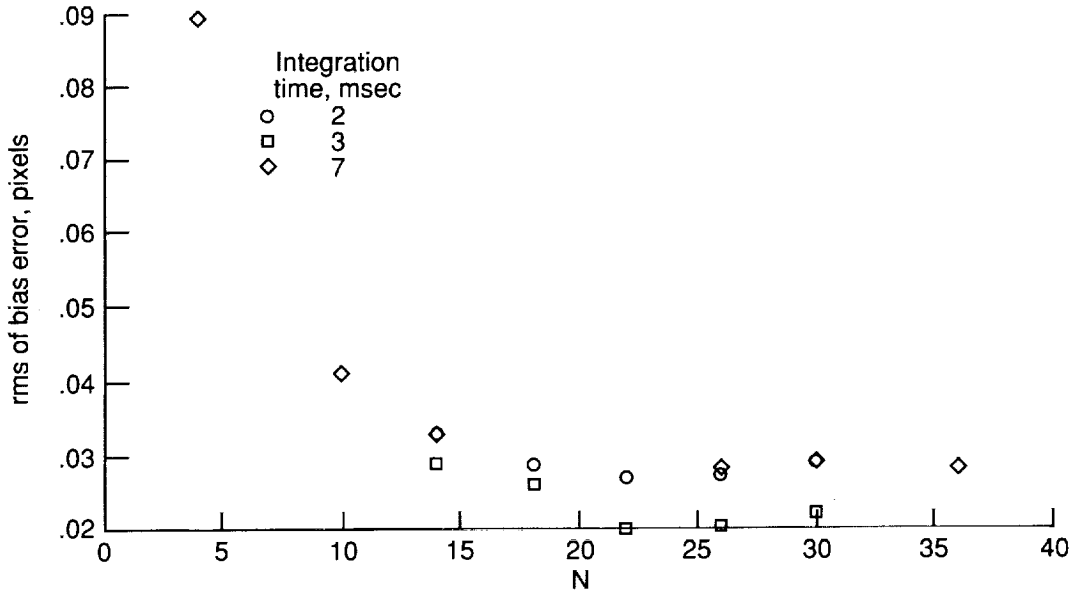

(b) Gaussian-shaped window.

Figure 17. Experimental rms of bias error as function of window size. Note the difference in vertical scale between the two plots.

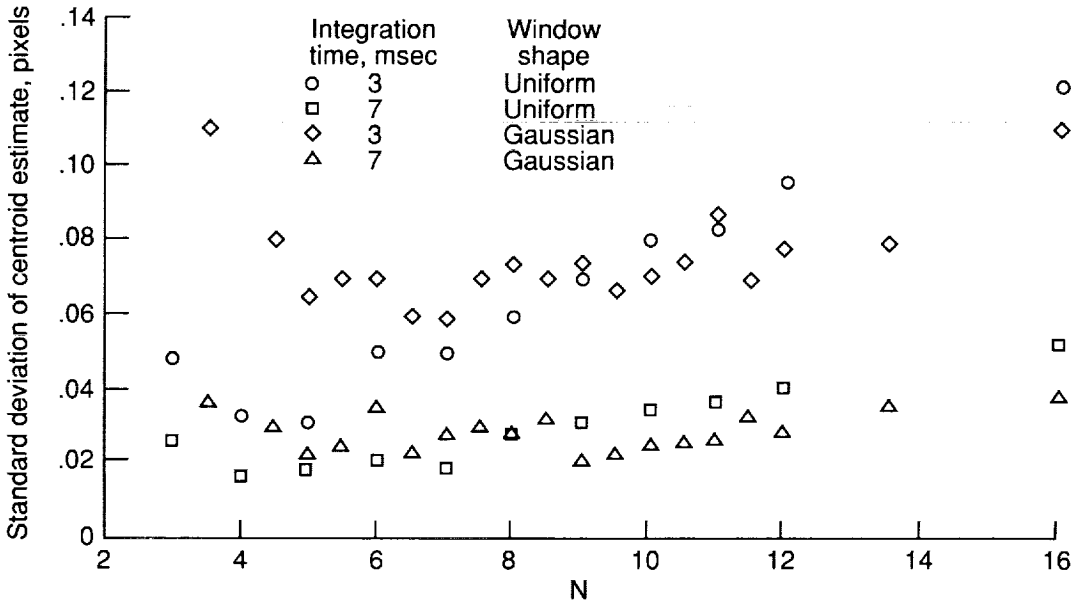

Figure 18. Experimental standard deviation of centroid estimate at single position of stage. Integration time was varied in order to vary effective SNR.

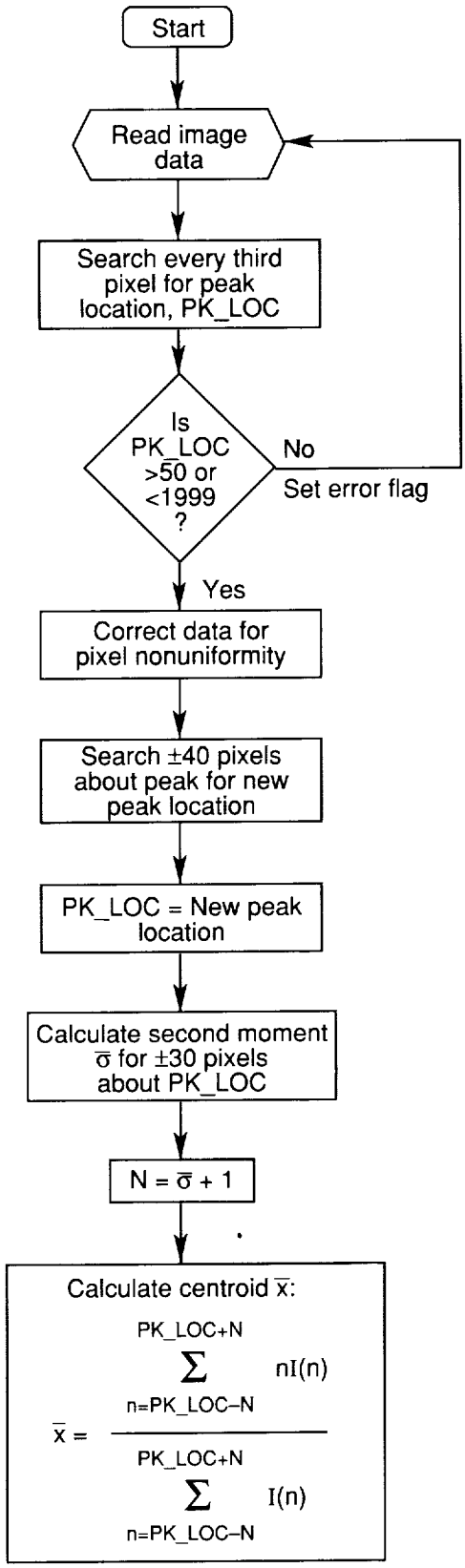

Figure 19. Flowchart of centroid-estimation algorithm.

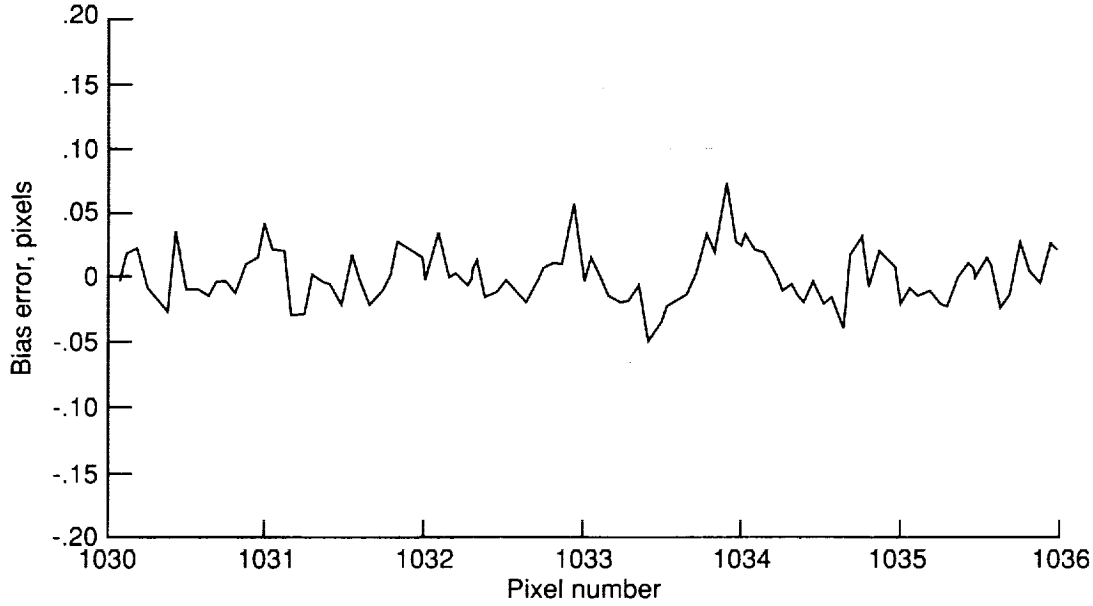

(a) SNR = 60.

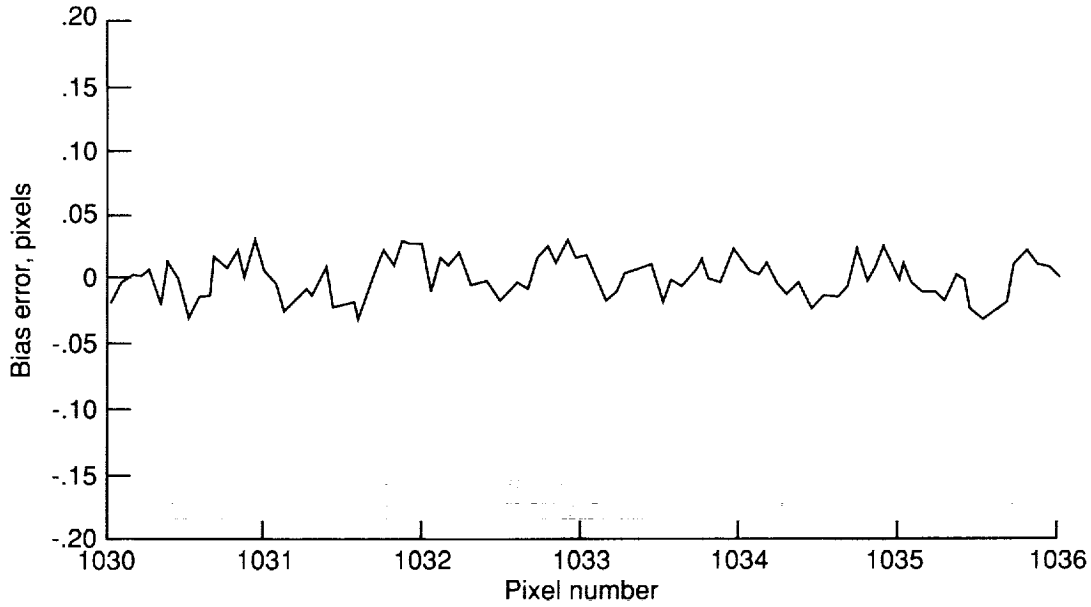

(b) SNR = 125.

Figure 20. Subpixel bias error from use of centroid-estimation algorithm that adjusts window size.

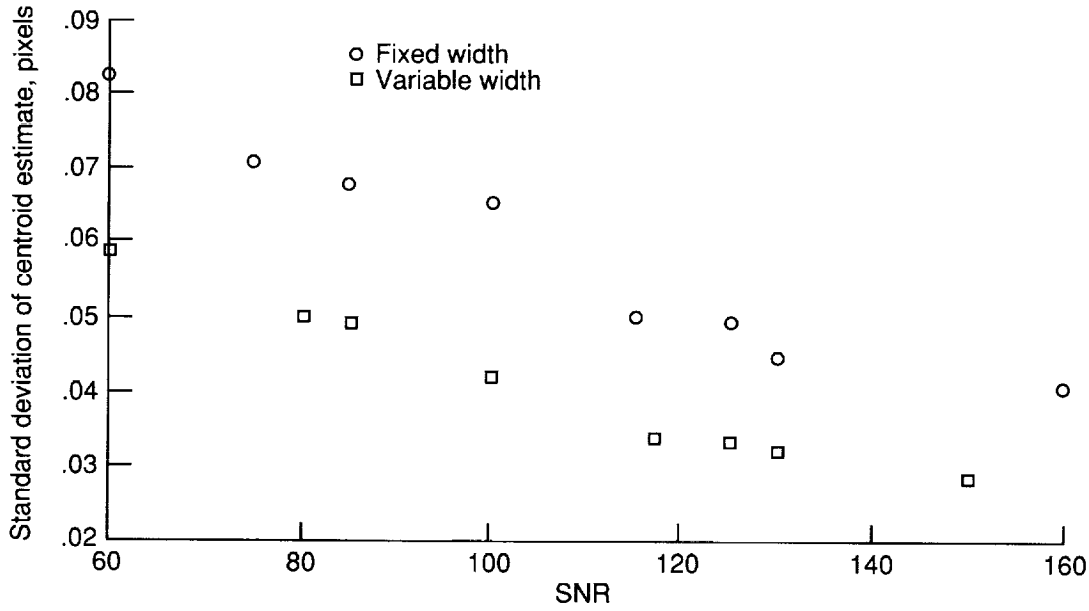

Figure 21. Standard deviation of centroid estimate versus SNR for uniform window of variable width and fixed width of $N = 14$.

REPORT DOCUMENTATION PAGE

Form Approved
OMB No. 0704-0188

1. AGENCY USE ONLY *(Leave blank)*	2. REPORT DATE	3. REPORT TYPE AND DATES COVERED
	October 1993	Technical Paper

4. TITLE AND SUBTITLE
Effects of Window Size and Shape on Accuracy of Subpixel Centroid Estimation of Target Images

5. FUNDING NUMBERS
WU 590-14-11-02

6. AUTHOR(S)
Sharon S. Welch

7. PERFORMING ORGANIZATION NAME(S) AND ADDRESS(ES)
NASA Langley Research Center
Hampton, VA 23681-0001

8. PERFORMING ORGANIZATION REPORT NUMBER
L-17113

9. SPONSORING/MONITORING AGENCY NAME(S) AND ADDRESS(ES)
National Aeronautics and Space Administration
Washington, DC 20546-0001

10. SPONSORING/MONITORING AGENCY REPORT NUMBER
NASA TP-3331

11. SUPPLEMENTARY NOTES

12a. DISTRIBUTION/AVAILABILITY STATEMENT
Unclassified–Unlimited

Subject Category 35

12b. DISTRIBUTION CODE

13. ABSTRACT *(Maximum 200 words)*

A new algorithm is presented for increasing the accuracy of subpixel centroid estimation of (nearly) point target images in cases where the signal-to-noise ratio is low and the signal amplitude and shape vary from frame to frame. In the algorithm, the centroid is calculated over a data window that is matched in width to the image distribution. Fourier analysis is used to explain the dependency of the centroid estimate on the size of the data window, and simulation and experimental results are presented which demonstrate the effects of window size for two different noise models. The effects of window shape have also been investigated for uniform and Gaussian-shaped windows. The new algorithm has been developed to improve the dynamic range of a close-range photogrammetric tracking system that provides feedback for control of a large gap magnetic suspension system (LGMSS).

14. SUBJECT TERMS	15. NUMBER OF PAGES
Centroid estimation; Target tracking; Charge-coupled device (CCD) sensors	36
	16. PRICE CODE A03

17. SECURITY CLASSIFICATION OF REPORT	18. SECURITY CLASSIFICATION OF THIS PAGE	19. SECURITY CLASSIFICATION OF ABSTRACT	20. LIMITATION OF ABSTRACT
Unclassified	Unclassified	Unclassified	

NSN 7540-01-280-5500

Standard Form 298(Rev. 2-89)
Prescribed by ANSI Std. Z39-18
298-102

National Aeronautics and
Space Administration
Code JTT
Washington, D.C.
20546-0001

Official Business
Penalty for Private Use, $300

BULK RATE
POSTAGE & FEES PAID
NASA
Permit No. G-27

NASA

POSTMASTER: If Undeliverable (Section 158 Postal Manual) Do Not Return